Improving Quantum Gate Performance through Neighboring Optimal Control

Yuchen Peng[1] and Frank Gaitan[2]

[1]*Department of Physics, University of Maryland, College Park, MD 20742*
[2]*Laboratory for Physical Sciences, 8050 Greenmead Dr, College Park, MD 20740*

(Dated: July 31, 2014)

Successful implementation of a fault-tolerant quantum computation on a system of qubits places severe demands on the hardware used to control the many-qubit state. It is known that an accuracy threshold P_a exists for any quantum gate that is to be used in such a computation. Specifically, the error probability P_e for such a gate must fall below the accuracy threshold: $P_e < P_a$. Estimates of P_a vary widely, though $P_a \sim 10^{-4}$ has emerged as a challenging target for hardware designers. In this paper we present a theoretical framework based on neighboring optimal control that takes as input a good quantum gate and returns a new gate with better performance. We illustrate this approach by applying it to all gates in a universal set of quantum gates produced using non-adiabatic rapid passage that has appeared in the literature. Performance improvements are substantial, both for ideal and non-ideal controls. Under suitable conditions detailed below, all gate error probabilities fall well below the target threshold of 10^{-4}.

PACS numbers: 03.67.Ac,03.67.Lx,42.50.Dv

arXiv:1407.8074v1 [quant-ph] 30 Jul 2014

I. INTRODUCTION

It is now well-established that reliable quantum computing is possible, even in the presence of decoherence and imperfect control [1–8]. In spite of this important result, it is also well-appreciated that significant technical obstacles currently stand in the way of building a scalable quantum computer. One major challenge is finding a way to implement a high-fidelity universal set of quantum gates from which an arbitrary quantum computation can be constructed. The accuracy threshold P_a provides a quantitative measure of the accuracy demanded of a quantum gate. Specifically, if a quantum gate is to be used in a reliable quantum computation, the probability P_e that it produces an error must be less than the accuracy threshold: $P_e < P_a$. The accuracy threshold is a function of the quantum error correcting code used to protect the computational data, and the fault-tolerant procedures used to control the spread of errors during the computation. Estimates of P_a vary widely, from as small as 10^{-6}, to as large as a few times 10^{-3}. Over the years, the value $P_a \sim 10^{-4}$ has emerged as a challenging target for quantum hardware designers. One of the central problems in quantum control is finding a way to implement a universal set of quantum gates whose gate error probabilities are all less than 10^{-4}.

To apply a quantum gate, a control field $\mathbf{F}(t)$ is applied to a quantum system over a time T, causing a time-varying unitary transformation $U(t)$ to act on the quantum state. When designing a quantum gate, the task is to find the control field $\mathbf{F}(t)$ that applies a target gate U_{tgt} to the quantum state (viz. $U(t = T) = U_{tgt}$). In optimal control theory, the task is to find a control field profile $\mathbf{F}_*(t)$ that produces a high-fidelity approximation $U(t)$ to the target gate U_{tgt}, while simultaneously minimizing a cost function that depends on the state $U(t)$ and control field $\mathbf{F}(t)$. The control profile $\mathbf{F}_*(t)$ is called the optimal control, and the corresponding unitary $U_*(t)$ is called the optimal (state) trajectory. Note that a perturbation of the dynamics can cause an optimal trajectory and control to become non-optimal. However, if the perturbation is small, the optimal control problem can be linearized about the original optimal solution, and a family of perturbed optimal trajectories determined from a single feedback control law. In the classical literature this perturbed control problem is referred to as neighboring optimal control [9].

In this paper we consider the problem of making a good quantum gate better. It is assumed that we know the control field profile $\mathbf{F}_0(t)$ that produces a good approximation $U_0(t = T)$ to a target gate U_{tgt}. We extend the strategy of neighboring optimal control to the dynamics of a quantum system and use it to determine the control modification $\Delta\mathbf{F}(t)$ that produces an improved approximation $U(t = T)$ to the target U_{tgt}. To illustrate the general theory, we use it to improve the performance of all gates in a universal set of quantum gates produced using non-adiabatic rapid passage that has been studied in the literature [10–17]. We examine both ideal and non-ideal controls, and show that under suitable conditions, all gate error probabilities fall well below the target threshold of 10^{-4}. Although we focus on a target threshold $P_a = 10^{-4}$ throughout this paper, it is important to note that for surface and color quantum error correcting codes, the accuracy threshold satisfies $P_a \sim 10^{-3}$ [18–22]. For these codes, the neighboring optimal control improved non-adiabatic rapid passage gates all operate at least two orders of magnitude below threshold, even for non-ideal control.

The structure of this paper is as follows. In Section II we lay out the general theoretical framework for applying neighboring optimal control to the problem of improving the performance of a good quantum gate. We use the Schrodinger equation to determine the equation of motion for the gate modification $\delta U(t) = U_0^{-1}(t)U(t)$ in Section II A; formulate the cost function for the opti-

mization in Section II B; derive the system of equations that determine the optimal solution in Section II C, and present two strategies for obtaining that solution in Section II D. We illustrate the general method in Section III by using it to improve the performance of a universal set of quantum gates. In the interests of clarity, Section III examines the case of the Hadamard gate in detail, with results for the remaining quantum gates presented in Appendix D. Finally, Section IV summarizes our results; Appendix A briefly reviews the form of non-adiabatic rapid passage used to produce the initial universal set of quantum gates examined in Section III; Appendix B derives a formula needed in Section II D; and Appendix C describes the noise model and simulation protocol used to examine phase jitter effects in Section III C 2.

II. GENERAL THEORY

In this Section we introduce a general theoretical framework that takes a good quantum gate $U_0(t)$ as input, and returns a better one $U(t)$. Section II A determines the equation of motion for the gate modification $\delta U(t) = U_0^\dagger(t)U(t)$; Section II B constructs the cost function whose minimum determines the optimal gate modification; Section II C varies the cost function to determine the equations that govern the optimization; and Section II D presents two strategies for obtaining their solution. In Section III we illustrate the general method by using it to improve the performance of all gates in a universal set of quantum gates.

In this paper we follow the standard physics convention of denoting a column vector by a boldface symbol $\mathbf{v}$; a row vector by the Hermitian adjoint of a boldface symbol $\mathbf{v}^\dagger$; and a matrix by a non-boldface symbol M. Thus $M\mathbf{v}$ represents the product of a matrix M with a column vector $\mathbf{v}$, and $\mathbf{y}^\dagger\mathbf{x}$ is the product of a row vector $\mathbf{y}^\dagger$ with a column vector $\mathbf{x}$.

A. Gate modification dynamics

Consider a Hamiltonian $H(t) = H[\mathbf{F}(t)]$ that is a functional of a control field $\mathbf{F}(t) = \mathbf{F}_0(t) + \Delta\mathbf{F}(t)$ that contains a small variation $\Delta\mathbf{F}(t)$ about a nominal control field $\mathbf{F}_0(t)$. Expanding the Hamiltonian $H(t)$ about $\mathbf{F}_0(t)$ gives

$$\begin{aligned} H(t) &= H[\mathbf{F}_0(t)] + \sum_{j=1}^{3} \left.\frac{\delta H}{\delta F_j}\right|_{\mathbf{F}_0} \Delta F_j + \mathcal{O}(\Delta^2) \\ &\equiv H_0(t) + \sum_{j=1}^{3} \mathcal{G}_j \Delta F_j(t), \end{aligned} \tag{1}$$

where $\mathcal{G}_j = \delta H/\delta F_j|_{\mathbf{F}_0}$ is an $N \times N$ matrix obtained by taking the functional derivative of $H[\mathbf{F}(t)]$ with respect to $F_j(t)$ evaluated at $\mathbf{F}_0(t)$, and N is the dimension of the Hilbert space. For example, suppose $H(t)$ is the Zeeman Hamiltonian $H(t) = -\boldsymbol{\sigma}\cdot\mathbf{F}(t)$, where the $1,2,3$ components of $\boldsymbol{\sigma}$ are the x, y, z Pauli matrices, respectively. Then, a simple calculation gives $\mathcal{G}_j = -\boldsymbol{\sigma}_j$.

The Schrodinger equation for the propagator $U(t)$ is ($\hbar = 1$)

$$i\frac{dU}{dt} = H(t)U. \tag{2}$$

For $H(t) = H[\mathbf{F}(t)]$, the propagator $U(t)$ becomes a functional of the control field $\mathbf{F}(t)$. Throughout this paper we assume that the nominal control field $\mathbf{F}_0(t)$ acts for a time T and gives rise to a propagator $U_0(t)$ which provides a good approximation $U_0(t=T)$ to a target gate U_{tgt} [23]. We introduce the gate modification $\delta U(t)$ by writing $U(t) = U_0(t)\delta U(t)$. Inserting Eq. (1) into Eq. (2), and substituting for $U(t)$ gives the equation of motion for $\delta U(t)$:

$$\begin{aligned} i\frac{d}{dt}\delta U &= \left[\sum_{j=1}^{3}\left(U_0^\dagger \mathcal{G}_j U_0\right)\Delta F_j\right]\delta U + \mathcal{O}(\Delta^2) \\ &= \left[\sum_{j=1}^{3}\overline{G}_j \Delta F_j\right]\delta U. \end{aligned} \tag{3}$$

Here $\overline{G}_j = U_0^\dagger(t)\mathcal{G}_j U_0(t)$ is an $N \times N$ matrix; and the initial condition $\delta U(0) = I$ follows from the definition of $\delta U(t)$ and $U(0) = U_0(0) = I$. By assumption, $U_0(t)$ already gives a good approximation to the target gate U_{tgt}, and so we look for a gate modification $\delta U(t)$ that is close to the identity: $\delta U(t) = I - i\delta A(t) + \mathcal{O}(\Delta^2)$. Note that $\delta A(t)$ is Hermitian, and $\delta A(0) = 0$. Substituting this expression for $\delta U(t)$ into Eq. (3) gives

$$\frac{d}{dt}\delta A = \sum_{j=1}^{3}\overline{G}_j \Delta F_j + \mathcal{O}(\Delta^2). \tag{4}$$

It proves useful to write the $N \times N$ matrix $\delta A(t)$ as an N^2-component column vector $\Delta\mathbf{x}(t)$. This is done by concatenating the columns $\{\delta A_{\bullet,j}(t) : j = 1, \cdots, N\}$ of $\delta A(t)$ into a single column vector:

$$\Delta\mathbf{x}(t) = \begin{pmatrix} \delta A_{\bullet,1}(t) \\ \vdots \\ \delta A_{\bullet,N}(t) \end{pmatrix}. \tag{5}$$

We also construct an $N^2 \times 3$ matrix $G(t)$ as follows. First we take each $N \times N$ matrix $\overline{G}_j(t)$ and convert it into an N^2-component column vector $\mathbf{G}_j(t)$ as described above. We then insert $\mathbf{G}_j(t)$ into the j-th column of $G(t)$:

$$G(t) = \begin{pmatrix} \vdots & \vdots & \vdots \\ \mathbf{G}_1(t) & \mathbf{G}_2(t) & \mathbf{G}_3(t) \\ \vdots & \vdots & \vdots \end{pmatrix}. \tag{6}$$

Finally, we introduce the column vector $\Delta\mathbf{F}(t)$:

$$\Delta\mathbf{F}(t) = \begin{pmatrix} \Delta F_1(t) \\ \Delta F_2(t) \\ \Delta F_3(t) \end{pmatrix}. \tag{7}$$

With these definitions, Eqn. (4) is transformed into the equation of motion for $\Delta\mathbf{x}(t)$:

$$\frac{d}{dt}\Delta\mathbf{x} \;=\; G(t)\Delta\mathbf{F}(t), \tag{8}$$

where the rhs is the matrix product of Eqs. (6) and (7), and the initial condition $\Delta\mathbf{x}(0) = 0$ follows from $\delta A(0) = 0$.

B. Dynamical optimization problem

In optimal control theory the problem is to determine a control field profile $\mathbf{F}_*(t)$ that optimizes system performance relative to a set of design criteria. A cost function is introduced that quantifies the degree to which a particular assignment of the control and system variables satisfies these criteria, with an optimal assignment being one of minimum cost [24]. The cost function J used in our gate optimization contains three contributions: (i) a terminal cost J_1 that vanishes when the final propagator $U(t = T)$ equals the target gate U_{tgt}; (ii) an integral cost J_2 that insures the control field and state modifications, respectively, $\Delta\mathbf{F}(t)$ and $\Delta\mathbf{y}(t)$ remain small at all times; and (iii) a Lagrange multiplier integral cost J_3 that insures the optimization does not violate the Schrodinger dynamics of $\Delta\mathbf{y}(t)$.

1. Terminal cost J_1: As shown in Ref. [14], and summarized in Appendix A,

$$Tr\, P = Tr\left[\left(U^\dagger(T) - U_{tgt}^\dagger\right)\left(U(T) - U_{tgt}\right)\right],$$

is a convenient upper bound on the gate error probability P_e which is clearly minimized when $U(T) = U_{tgt}$. We will use it as a terminal cost:

$$J_1 \;=\; Tr\left[\left(U^\dagger(T) - U_{tgt}^\dagger\right)\left(U(T) - U_{tgt}\right)\right]. \tag{9}$$

The cost J_1 enforces the criterion that $U(T) = U_{tgt}$ softly, allowing it to be violated, but penalizing violations with non-zero cost. By assumption, $U_0(T)$ is a good approximation for U_{tgt}, and so $U_0^\dagger(T)U_{tgt} = I - i\delta\beta + \mathcal{O}(\Delta^2)$, where $\delta\beta$ is Hermitian. Recall that $U(t) = U_0(t)\delta U(t)$ and $\delta U(t) = I - i\delta A(t) + \mathcal{O}(\Delta^2)$. Expanding J_1 to second order gives:

$$J_1 = Tr\left[\left(\delta A^\dagger(T) - \delta\beta^\dagger\right)\left(\delta A(T) - \delta\beta\right)\right]. \tag{10}$$

If we write $\delta\beta$ as a (constant) N^2-component vector $\Delta\boldsymbol{\beta}$ as was done with $\delta A(t)$ in Eq. (5), we can re-write J_1 as the product of a row and column vector

$$J_1 = \left(\Delta\mathbf{x}^\dagger(T) - \Delta\boldsymbol{\beta}^\dagger\right)\left(\Delta\mathbf{x}(T) - \Delta\boldsymbol{\beta}\right). \tag{11}$$

Defining the column vector $\Delta\mathbf{y}(t)$ as

$$\Delta\mathbf{y}(t) = \Delta\mathbf{x}(t) - \Delta\boldsymbol{\beta}, \tag{12}$$

J_1 becomes the square-magnitude of $\Delta\mathbf{y}(T)$

$$J_1 = \Delta\mathbf{y}^\dagger(T)\Delta\mathbf{y}(T). \tag{13}$$

Note that since $\Delta\boldsymbol{\beta}$ is a constant vector, $\Delta\mathbf{y}(t)$ also satisfies Eq. (8):

$$\frac{d}{dt}\Delta\mathbf{y} = G\Delta\mathbf{F}. \tag{14}$$

The initial condition for Eq. (14) is $\Delta\mathbf{y}(0) = -\Delta\boldsymbol{\beta}$ which follows from Eq. (12) and $\Delta\mathbf{x}(0) = 0$. It proves convenient in the following to work with $\Delta\mathbf{y}(t)$ instead of $\Delta\mathbf{x}(t)$.

2. Integral cost J_2: The second cost term J_2 is an integral cost that penalizes large values of $\Delta\mathbf{F}(t)$ and $\Delta\mathbf{y}(t)$ for all times t:

$$J_2 = \int_0^T dt\left[\Delta\mathbf{y}^\dagger(t)Q(t)\Delta\mathbf{y}(t) + \frac{1}{2}\Delta\mathbf{F}^T(t)R(t)\Delta\mathbf{F}(t)\right]. \tag{15}$$

Here $Q(t)$ and $R(t)$ are positive-definite Hermitian matrices, but otherwise, are at our disposal [25]. The cost J_2 is minimized by vanishing state and control modifications $\Delta\mathbf{y}(t) = 0$ and $\Delta\mathbf{F}(t) = 0$. Non-vanishing $\Delta\mathbf{y}(t)$ and $\Delta\mathbf{F}(t)$ are allowed to occur, but they are penalized with non-zero cost. Thus J_2 acts to softly enforce the criterion of small state and control modifications.

3. Integral cost J_3: Finally, we require that the optimization obey the Schrodinger dynamics of $\Delta\mathbf{y}(t)$. This criterion is enforced as a hard constraint which cannot be violated by introducing a Lagrange multiplier $\Delta\boldsymbol{\lambda}(t)$:

$$\begin{aligned} J_3 \;&=\; \int_0^T dt\left[\Delta\boldsymbol{\lambda}^\dagger(t)\left\{G(t)\Delta\mathbf{F}(t) - \Delta\dot{\mathbf{y}}(t)\right\} + h.\,c.\right] \\ &=\; -\,\Delta\boldsymbol{\lambda}^\dagger\Delta\mathbf{y}\Big|_0^T \\ &\qquad + \int_0^T dt\left[\left(\Delta\boldsymbol{\lambda}^\dagger(t)G(t)\Delta\mathbf{F}(t) + \Delta\dot{\boldsymbol{\lambda}}^\dagger(t)\Delta\mathbf{y}(t)\right)\right. \\ &\qquad\qquad \left. + h.\,c.\right]. \end{aligned} \tag{16}$$

Note that we have done an integration by parts in going from the first to the second line; a dot over a symbol indicates a time-derivative; and $h.\,c.$ indicates the Hermitian conjugate of the preceeding term.

4. Total cost J: Combining all three costs gives

$$\begin{aligned} J \;&=\; \left[\Delta\mathbf{y}^\dagger(T)\Delta\mathbf{y}(T) - \Delta\boldsymbol{\lambda}^\dagger(T)\Delta\mathbf{y}(T)\right] \\ &\qquad + \int_0^T dt\left[\Delta\mathbf{y}^\dagger(t)Q(t)\Delta\mathbf{y}(t) + \frac{1}{2}\Delta\mathbf{F}^T R(t)\Delta\mathbf{F}(t)\right] \\ &\qquad + \int_0^T dt\left[\left(\Delta\dot{\boldsymbol{\lambda}}^\dagger(t)\Delta\mathbf{y}(t) + \Delta\boldsymbol{\lambda}^\dagger(t)G(t)\Delta\mathbf{F}(t)\right)\right. \\ &\qquad\qquad \left. + h.\,c.\right]. \end{aligned} \tag{17}$$

As we shall see in Section II C, appropriate variation of J gives the equations that govern the optimization, including the feedback control law. Note that we have dropped the $\Delta\boldsymbol{\lambda}^\dagger(0)\Delta\mathbf{y}(0)$ contribution to J that arises from the surface term in Eq. (16) as it has zero variation since $\Delta\mathbf{y}(0) = -\Delta\boldsymbol{\beta}$ is a constant with zero variation.

C. Euler-Lagrange equations for optimal control

A necessary condition for optimal control is that the first-order variation of the cost function J vanish. This is most easily worked out by taking functional derivatives of J with respect to $\Delta\mathbf{y}(t)$, $\Delta\mathbf{F}(t)$, and $\Delta\boldsymbol{\lambda}(t)$, and setting these derivatives equal to zero. This leads to the equations of motion that govern the optimization. It follows automatically from the positive-definite quadratic nature of J that its second-order variation is positive, making the extremum solution found from the first-order variation the desired minimum cost solution.

1. Variation of $\Delta\mathbf{y}(t)$: Taking the functional derivative of J with respect to $\Delta\mathbf{y}(T)$ and setting the result equal to zero gives

$$\Delta\mathbf{y}^\dagger(T) - \Delta\boldsymbol{\lambda}^\dagger(T) = 0.$$

Solving for $\Delta\boldsymbol{\lambda}(T)$ gives:

$$\Delta\boldsymbol{\lambda}(T) = \Delta\mathbf{y}(T). \tag{18}$$

Next, taking the functional derivative of J with respect to $\Delta\mathbf{y}(t)$ and setting the result equal to zero gives

$$\Delta\mathbf{y}^\dagger(t)Q(t) + \Delta\dot{\boldsymbol{\lambda}}^\dagger(t) = 0.$$

Solving for $\Delta\dot{\boldsymbol{\lambda}}(t)$ gives (recall $Q(t)$ is Hermitian):

$$\frac{d}{dt}\Delta\boldsymbol{\lambda}(t) = -Q(t)\Delta\mathbf{y}(t). \tag{19}$$

Eqs. (18) and (19) define an initial value problem for the Lagrange multiplier $\Delta\boldsymbol{\lambda}(t)$, where the "initial" time is $t = T$. Note that taking the functional derivative of J with respect to $\Delta\mathbf{y}^\dagger(t)$ simply gives the adjoint of these equations and so provides no new information.

2. Variation of $\Delta\mathbf{F}(t)$: Taking the functional derivative of J with respect to $\Delta\mathbf{F}(t)$ and setting it equal to zero gives:

$$\Delta\mathbf{F}^T(t)R(t) + \Delta\boldsymbol{\lambda}^\dagger G(t) = 0.$$

Solving for $\Delta\mathbf{F}(t)$ gives (recall $R(t)$ is positive-definite and Hermitian):

$$\Delta\mathbf{F}(t) = -R^{-1}(t)G^\dagger(t)\Delta\boldsymbol{\lambda}(t). \tag{20}$$

Eq. (20) relates the control modification $\Delta\mathbf{F}(t)$ to the Lagrange multiplier $\Delta\boldsymbol{\lambda}(t)$. Note that for the second strategy presented in Section II D, this equation will be transformed into a feedback control law.

3. Variation of $\Delta\boldsymbol{\lambda}(t)$: By design, J_3 was added to the cost function to insure that the Schrodinger dynamics of $\Delta\mathbf{y}(t)$ is not violated by the optimization process. Taking the functional derivative of the first line of Eq. (16) and setting the result equal to zero gives

$$\frac{d}{dt}\Delta\mathbf{y}(t) - G(t)\Delta\mathbf{F}(t) = 0, \tag{21}$$

which is Eq. (14) as required. We have already seen that its initial condition is

$$\Delta\mathbf{y}(0) = -\Delta\boldsymbol{\beta}. \tag{22}$$

D. Solution strategies

Here we describe two strategies for solving the Euler-Lagrange equations of motion for optimal control (Eqs. (18)-(22)). Each strategy provides a way to determine $\Delta\boldsymbol{\lambda}(t)$ without directly integrating Eqs. (18)–(19). The first is based on an ansatz for the Lagrange multiplier $\Delta\boldsymbol{\lambda}(t)$, while the second relates $\Delta\boldsymbol{\lambda}(t)$ to $\Delta\mathbf{y}(t)$ through the Ricatti matrix $S(t)$.

In Section III and Appendix D we use our neighboring optimal control formalism to improve the performance of all gates in the universal set of gates introduced in Appendix A 3. Strategy 1 will be used to improve all one-qubit gates, while Strategy 2 will be used to improve the sole two-qubit gate in the set.

Strategy 1 – Lagrange multiplier ansatz: This approach to solving the Euler-Lagrange (EL) equations for optimal control is based on the following ansatz for the Lagrange multiplier:

$$\Delta\boldsymbol{\lambda}(t) = -\exp\left[-(t + t_0/2)/10\right]\mathbf{w}, \tag{23}$$

where $-T/2 \le t \le T/2$, and $\mathbf{w}$ is a constant vector that is determined by demanding that: (i) the gate modification $\delta A(t) = i[\delta U(t) - I]$ satisfies the Schrodinger equation (viz. Eq. (4)); and (ii) $\delta A(T/2) = \delta\beta + \mathcal{O}(\Delta^2)$, where $\delta\beta = i[U_0^\dagger(T/2)U_{tgt} - I] + \mathcal{O}(\Delta^2)$ (see Section II B). Note that, because of the second requirement,

$$\begin{aligned}\delta U(T/2) &= I - i\delta A(T/2) + \mathcal{O}(\Delta^2)\\ &= I - i\delta\beta + \mathcal{O}(\Delta^2)\\ &= U_0^\dagger(T/2)U_{tgt} + \mathcal{O}(\Delta^2),\end{aligned}$$

and consequently, the new gate $U(T/2) = U_0(T/2)\delta U(T/2)$ satisfies:

$$\begin{aligned}U(T/2) &= U_0(T/2)\left[U_0^\dagger(T/2)U_{tgt}\right]\\ &= U_{tgt} + \mathcal{O}(\Delta^2).\end{aligned} \tag{24}$$

Thus, by choosing $\mathbf{w}$ in this way, we insures that EL Eqs. (21) and 22) are satisfied, and the new gate $U(T/2)$ is the target gate U_{tgt} to second-order in small quantities.

We choose $R(t) = I$ so that Eq. (20) gives the control modification:

$$\Delta\mathbf{F}(t) = \exp\left[-(t+T/2)/10\right] G^\dagger(t)\mathbf{w}. \tag{25}$$

Once $\mathbf{w}$ is determined, EL Eq. (20) is satisfied.

Finally, choosing $Q(t)$ to be a diagonal matrix, Eq. (19) determines $Q(t)$ from the ansatz for $\Delta\boldsymbol{\lambda}(t)$ and the solution $\Delta\mathbf{y}(t)$ of Eqs. (21) and (22). With this choice, EL Eq. (19) is satisfied. Thus, once $\mathbf{w}$ is known, the strategy's construction insures that all EL equations are satisfied, and yields the control and gate modifications $\Delta\mathbf{F}(t)$ and $\Delta\mathbf{y}(t)$. Note that Strategy 1 has the following significant benefit. By introducing an ansatz for $\Delta\boldsymbol{\lambda}(t)$, computation of the control and gate modifications $\Delta\mathbf{F}(t)$ and $\Delta\mathbf{y}(t)$ becomes independent of $Q(t)$. Thus Strategy 1 does not actually require $Q(t)$ to be computed. We now describe how $\mathbf{w}$ is determined.

We begin with Eq. (4), together with Eq. (25):

$$\begin{aligned}\frac{d}{dt}\delta A &= \sum_{j=1}^{3} \overline{G}_j \Delta F_j \\ &= \exp\left[-(t+T/2)/10\right] \sum_{j=1}^{3} \overline{G}_j \left(G^\dagger\mathbf{w}\right)_j . \end{aligned} \tag{26}$$

In Appendix B we show that

$$\sum_{j=1}^{3} \overline{G}_j \left(G^\dagger\mathbf{w}\right)_j = \begin{pmatrix} w_1 - w_4 & 2w_3 \\ 2w_2 & w_4 - w_1 \end{pmatrix}. \tag{27}$$

Note that in deriving this result we explicitly assume that our quantum system is a single qubit whose dynamics is driven by the Zeeman Hamiltonian $H(t) = -\boldsymbol{\sigma}\cdot\mathbf{F}(t)$. Using Eq. (27) in Eq. (26) gives

$$\begin{aligned}&\frac{d}{dt}\begin{pmatrix} \delta A_{11} & \delta A_{12} \\ \delta A_{21} & \delta A_{22} \end{pmatrix} = \\ &\qquad \exp\left[-(t+T/2)/10\right] \begin{pmatrix} w_1 - w_4 & 2w_3 \\ 2w_2 & w_4 - w_1 \end{pmatrix}. \end{aligned} \tag{28}$$

This equation is easily integrated, with the result:

$$\delta A_{11}(t) = 10\,(w_1 - w_4)\,\mathcal{A}(t) \tag{29a}$$
$$\delta A_{21}(t) = 20 w_2\,\mathcal{A}(t) \tag{29b}$$
$$\delta A_{12}(t) = 20 w_3\,\mathcal{A}(t) \tag{29c}$$
$$\delta A_{22}(t) = 10\,(w_4 - w_1)\,\mathcal{A}(t), \tag{29d}$$

where

$$\mathcal{A}(t) = 1 - \exp\left[-(t+T/2)/10\right]. \tag{30}$$

For the one-qubit gate simulations presented in Section III and Appendix D we have $T = 160$ [26]. Thus $\mathcal{A}(T/2) = 1 - \exp(-16) = 1 + \mathcal{O}(10^{-7})$. Combining this with the requirement that $\delta A(T/2) = \delta\beta$ gives

$$w_1 - w_4 = \frac{\delta\beta_{11}}{10} \tag{31a}$$
$$w_2 = \frac{\delta\beta_{21}}{20} \tag{31b}$$
$$w_3 = \frac{\delta\beta_{12}}{20} \tag{31c}$$
$$w_4 - w_1 = \frac{\delta\beta_{22}}{10}. \tag{31d}$$

Recall that $U_0^\dagger(T/2)U_{tgt} = I - i\delta\beta + \mathcal{O}(\Delta^2)$ so that

$$\begin{aligned} Tr\left[U_0^\dagger(T/2)U_{tgt}\right] &= 2 - i\,Tr\,\delta\beta + \mathcal{O}(\Delta^2) \\ &= 2 - i\left(\delta\beta_{11} + \delta\beta_{22}\right) + \mathcal{O}(\Delta^2). \end{aligned} \tag{32}$$

In Appendix A 3 we show that for all one-qubit gates of interest in this paper, $Tr\left[U_0^\dagger(T/2)U_{tgt}\right] = 2 + \mathcal{O}(\Delta^2)$ so that

$$\delta\beta_{11} + \delta\beta_{22} = 0. \tag{33}$$

Combining Eq. (33) with the choice $w_1 = -w_4$, reduces Eqs. (31) to

$$\mathbf{w} = \frac{\Delta\boldsymbol{\beta}}{20}, \tag{34}$$

where, recall,

$$\Delta\boldsymbol{\beta} = \begin{pmatrix} \delta\beta_{11} \\ \delta\beta_{21} \\ \delta\beta_{12} \\ \delta\beta_{22} \end{pmatrix}. \tag{35}$$

Eqs. (34) and (35), together with $\delta\beta = i[U_0^\dagger(T/2)U_{tgt} - I]$, determine $\mathbf{w}$. As was noted above, this then determines the control modification $\Delta\mathbf{F}(t)$, and solution of the Schrodinger equation determines $\Delta\mathbf{y}(t)$ which gives the gate modification $\delta U(t)$. The new control field is $\mathbf{F}(t) = \mathbf{F}_0(t) + \Delta\mathbf{F}(t)$, and the new gate is $U(T/2) = U_0(T/2)\delta U(T/2)$. We implement Strategy 1 in Section III and Appendix D to improve the one-qubit gates in the universal quantum gate set introduced in Appendix A 3.

Strategy 2 – Ricatti equation and the control gain matrix: From Eq. (19) we see that $\Delta\mathbf{y}(t)$ acts as the source for the Lagrange multiplier $\Delta\boldsymbol{\lambda}(t)$. We look for a solution of Eq. (19) of the form

$$\Delta\boldsymbol{\lambda}(t) = S(t)\Delta\mathbf{y}(t), \tag{36}$$

where $S(t)$ is known as the Ricatti matrix. Note that once $S(t)$ has been determined, Eq. (20) becomes the feedback control law

$$\begin{aligned}\Delta\mathbf{F}(t) &= -R^{-1}(t)G^\dagger(t)S(t)\Delta\mathbf{y}(t) \\ &= -C(t)\Delta\mathbf{y}(t) \end{aligned} \tag{37}$$

which relates the state modification $\Delta\mathbf{y}(t)$ to the control modification $\Delta\mathbf{F}(t)$. The matrix $C(t) = R^{-1}(t)G^\dagger(t)S(t)$ is known as the control gain matrix. To obtain the equation of motion for $S(t)$ we differentiate Eq. (36), and then use Eqs. (19) and (21) to substitute for $\Delta\dot{\boldsymbol{\lambda}}$ and $\Delta\dot{\mathbf{y}}$. One finds

$$\begin{aligned}\dot{S}\Delta\mathbf{y} &= \Delta\dot{\boldsymbol{\lambda}} - S\Delta\dot{\mathbf{y}} \\ &= -Q\Delta\mathbf{y} - SG\Delta\mathbf{F} \\ &= -Q\Delta\mathbf{y} - SG(-R^{-1}G^\dagger S\Delta\mathbf{y}) \\ &= \left[-Q + SGR^{-1}G^\dagger S\right]\Delta\mathbf{y}. \end{aligned} \tag{38}$$

Identifying the coefficients of $\Delta\mathbf{y}$ on both sides of Eq. (38) gives the Ricatti equation

$$\frac{dS}{dt} = -Q + SGR^{-1}G^\dagger S. \tag{39}$$

The "initial" condition for $S(T)$ is found from Eqs. (18) and (36):

$$\Delta\mathbf{y}(T) = S(T)\Delta\mathbf{y}(T),$$

from which it follows that

$$S(T) = I. \tag{40}$$

Note that by introducing the Ricatti matrix $S(t)$ we have transformed the problem of finding the Lagrange multiplier $\Delta\boldsymbol{\lambda}(t)$ to that of finding $S(t)$. This is a good strategy as the Ricatti equation is independent of both $\Delta\mathbf{y}(t)$ and $\Delta\mathbf{F}(t)$ and so can be solved once and for all. This is not the case with Eq. (19). The equations that determine the path and control modifications $\Delta\mathbf{y}(t)$ and $\Delta\mathbf{F}(t)$ are thus Eqs. (12), (21), (22), (37), (39), and (40). Note that by substituting the feedback control law (Eq. (37)) into Eq. (21) we obtain

$$\frac{d}{dt}\Delta\mathbf{y} = -GC\Delta\mathbf{y}. \tag{41}$$

Once the Ricatti matrix $S(t)$ is known, the control gain matrix $C(t)$ is known, and Eq. (41) can then be integrated for $\Delta\mathbf{y}(t)$. With $\Delta\mathbf{y}(t)$ in hand, Eq. (37) determines the control modification $\Delta\mathbf{F}(t)$, and so the improved control $\mathbf{F}(t) = \mathbf{F}_0(t) + \Delta\mathbf{F}(t)$. Note that if all the eigenvalues of GC are positive, then $\Delta\mathbf{y}(t \to \infty) = 0$, and so from Eq. (12), that $\Delta\mathbf{x}(t \to \infty) = \Delta\boldsymbol{\beta}$. This, in turn implies that $\delta U(t \to \infty) = U_0^\dagger U_{tgt}$, and finally, $U(t \to \infty) = U_{tgt}$ as desired.

III. EXAMPLE: IMPROVING A UNIVERSAL QUANTUM GATE SET

Having constructed in Section II a general theoretical framework for improving the performance of a good quantum gate, we now illustrate its use by applying it to a universal set of quantum gates that has appeared in the literature [10–17]. These gates are implemented using a form of non-adiabatic rapid passage known as twisted rapid passage (TRP). We stress that the method introduced in Section II is not limited to this particular family of input gates - any other good gate, or set of gates, could serve as the input for the method. As noted earlier, in the interests of clarity, we focus on the Hadamard gate in this Section, and present our results for the remaining quantum gates in this set in Appendix D.

A. Twisted Rapid Passage

In an effort to make this paper more self-contained, we briefly review the needed background material on twisted rapid passage (TRP). For a more detailed presentation, the reader is directed to Refs. [10, 14–16], as well as Appendix A below.

1. TRP and Controllable Quantum Interference

To introduce TRP [10, 14], we consider a single-qubit interacting with an external control-field $\mathbf{F}(t)$ via the Zeeman interaction $H_z(t) = -\boldsymbol{\sigma}\cdot\mathbf{F}(t)$, where σ_i are the Pauli matrices ($i = x, y, z$). TRP is a generalization of adiabatic rapid passage (ARP) [27]. In ARP, the control-field $\mathbf{F}(t)$ is slowly inverted over a time T with $\mathbf{F}(t) = at\,\hat{\mathbf{z}} + b\,\hat{\mathbf{x}}$. In TRP, however, the control-field is allowed to twist in the x-y plane with time-varying azimuthal angle $\phi(t)$, while simultaneously undergoing inversion along the z-axis: $\mathbf{F}_0(t) = at\,\hat{\mathbf{z}} + b\cos\phi(t)\,\hat{\mathbf{x}} + b\sin\phi(t)\,\hat{\mathbf{y}}$. Here $-T/2 \le t \le T/2$, and throughout this paper, we consider TRP with *non-adiabatic* inversion. As shown in Ref. [14], the qubit undergoes resonance when

$$at - \frac{\hbar}{2}\frac{d\phi}{dt} = 0. \tag{42}$$

For polynomial twist, the twist profile $\phi(t)$ takes the form

$$\phi_n(t) = \frac{2}{n}Bt^n. \tag{43}$$

In this case, Eq. (42) has $n-1$ roots, though only real-valued roots correspond to resonance. Ref. [10] showed that for $n \ge 3$, the qubit undergoes resonance multiple times during a *single* TRP sweep: (i) for all $n \ge 3$, when $B > 0$; and (ii) for odd $n \ge 3$, when $B < 0$. For the remainder of this paper we restrict ourselves to $B > 0$, and to *quartic* twist for which $n = 4$ in Eq. (43). During quartic twist, the qubit passes through resonance at times $t = 0, \pm\sqrt{a/\hbar B}$ [10]. It is thus possible to alter the time separating the resonances by varying the TRP sweep parameters B and a.

Ref. [10] showed that these multiple resonances have a strong influence on the qubit transition probability, allowing transitions to be strongly enhanced or suppressed through a small variation of the sweep parameters. Ref. [28] calculated the qubit transition amplitude

to all orders in the non-adiabatic coupling. The result found there can be re-expressed as the following diagrammatic series:

$T_-(t)$ =

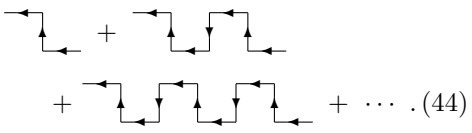

(44)

Lower (upper) lines correspond to propagation in the negative (positive) energy-level, and the vertical lines correspond to transitions between the two energy-levels. The calculation sums the probability amplitudes for all interfering alternatives [29] that allow the qubit to end up in the positive energy-level given that it was initially in the negative energy-level. As we have seen, varying the TRP sweep parameters varies the time separating the resonances. This in turn changes the value of each diagram in Eq. (44), and thus alters the interference between the alternative transition pathways. It is the sensitivity of the individual alternatives/diagrams to the time separation of the resonances that allows TRP to manipulate this quantum interference. Zwanziger et al. [11] observed these interference effects in the transition probability using NMR and found excellent quantitative agreement between theory and experiment. It is this link between interfering quantum alternatives and the TRP sweep parameters that we believe underlies the ability of TRP to drive high-fidelity non-adiabatic one- and two-qubit gates.

2. Universal Quantum Gate Set

The universal set of quantum gates $\mathcal{G}_U$ that is of interest here consists of the one-qubit Hadamard and NOT gates, together with variants of the one-qubit $\pi/8$ and phase gates, and the two-qubit controlled-phase gate. Operator expressions for these gates are: (1) Hadamard: $U_h = (1/\sqrt{2})\,(\,\sigma_z + \sigma_x)$; (2) NOT: $U_{not} = \sigma_x$; (3) Modified $\pi/8$: $V_{\pi/8} = \cos(\pi/8)\;\sigma_x - \sin(\pi/8)\;\sigma_y$; (4) Modified phase: $V_p = (1/\sqrt{2})\,(\,\sigma_x - \sigma_y\,)$; and (5) Modified controlled-phase: $V_{cp} = (1/2)\left[\left(I^1 + \sigma_z^1\right) I^2 - \left(I^1 - \sigma_z^1\right)\sigma_z^2\right]$. The universality of $\mathcal{G}_U$ was demonstrated in Ref. [15] by showing that its gates could construct the well-known universal set comprised of the Hadamard, phase, $\pi/8$, and CNOT gates.

3. Simulation Procedure

As is well-known, the Schrodinger dynamics is driven by a Hamiltonian $H(t)$ that causes a unitary transformation $U(t, t_0)$ to be applied to an initial quantum state $|\psi(t_0)\rangle$. In this paper, it is assumed that the Hamiltonian $H(t)$ contains terms that Zeeman-couple each qubit to the TRP control-field $\mathbf{F}_0(t)$. Assigning values to the TRP sweep parameters (a, b, B, T) fixes the control-field $\mathbf{F}_0(t)$, and in turn, the actual unitary transformation $U_a = U(t_0 + T, t_0)$ applied to $|\psi(t_0)\rangle$. Ref. [15] used optimization algorithms to find TRP sweep parameter values that produced an applied one-qubit (two-qubit) gate U_a that approximates a desired target gate U_{tgt} sufficiently closely that its error probability (defined below) satisfies $P_e < 10^{-4}$ (10^{-3}) [30]. In the following, the target gate U_{tgt} will be one of the gates in the universal set $\mathcal{G}_U$. Since $\mathcal{G}_U$ contains only one- and two-qubit gates, our simulations will only involve one- and two-qubit systems.

For the *one-qubit simulations*, the nominal Hamiltonian $H_0^1(t)$ is the Zeeman Hamiltonian $H_z(t)$ introduced in Section III A 1. Ref. [14] (see also Appendix A) showed that it can be written in the following dimensionless form:

$$\begin{aligned} H_0^1(\tau) &= (1/\lambda)\,\{-\tau\sigma_z - \cos\phi_4(\tau)\sigma_x - \sin\phi_4(\tau)\sigma_y\} \\ &= -\boldsymbol{\sigma}\cdot\mathbf{F}_0(\tau), \end{aligned} \tag{45}$$

where $\mathbf{F}_0(\tau)$ is the dimensionless TRP control field; $\tau = (a/b)t$; $\lambda = \hbar a/b^2$; and for quartic twist, $\phi_4(\tau) = (\eta_4/2\lambda)\tau^4$, with $\eta_4 = \hbar B b^2/a^3$. In this Section, we show how the neighboring optimal control framework introduced in Section II is applied to improve the performance of the TRP-generated Hadamard gate. As the implementation for the remaining one-qubit TRP gates is similar, for reasons of clarity, we defer their discussion to Appendix D.

For the *two-qubit simulations*, the nominal Hamiltonian $H_0^2(t)$ contains terms that Zeeman-couple each qubit to the TRP control-field $\mathbf{F}_0(t)$, and an Ising interaction term that couples the two qubits. Alternative two-qubit interactions can easily be considered, though all simulation results presented in this paper assume an Ising interaction between the qubits. To break a resonance-frequency degeneracy $\omega_{12} = \omega_{34}$ for transitions between, respectively, the ground and first-excited states $(E_1 \leftrightarrow E_2)$ and the second- and third-excited states $(E_3 \leftrightarrow E_4)$, the term $c_4|E_4(t)\rangle\langle E_4(t)|$ was added to $H_2(t)$. Combining all of these remarks, we arrive at the following (dimensionless) two-qubit Hamiltonian (see Ref. [15] or Appendix A for further details):

$$\begin{aligned} H_0^2(\tau) = {} & [-(d_1+d_2)/2 + \tau/\lambda]\,\sigma_z^1 \\ & + [-d_2/2 + \tau/\lambda]\,\sigma_z^2 \\ & - (d_3/\lambda)\left[\cos\phi_4\sigma_x^1 + \sin\phi_4\sigma_y^1\right] \\ & - (1/\lambda)\left[\cos\phi_4\sigma_x^2 + \sin\phi_4\sigma_y^2\right] \\ & - (\pi d_4/2)\sigma_z^1\sigma_z^2 \quad + c_4|E_4(\tau)\rangle\langle E_4(\tau)|. \end{aligned} \tag{46}$$

Here: (i) $b_i = \hbar\gamma_i B_{rf}/2$, $\omega_i = \gamma_i B_0$, γ_i is the coupling constant for qubit i, and $i = 1, 2$; (ii) $\tau = (a/b_2)t$, $\lambda = \hbar a/b_2^2$, and $\eta_4 = \hbar B b_2^2/a^3$; and (iii) $d_1 = (\omega_1 - \omega_2)b_2/a$, $d_2 = (\Delta/a)b_2$, $d_3 = b_1/b_2$, and $d_4 = (J/a)b_2$, where Δ is a detuning parameter. In the interests of clarity, we present our results for the two-qubit modified controlled phase gate in Appendix D.

Given an applied gate U_a, a target gate U_{tgt}, and the initial state $|\psi\rangle$, it is possible to determine (see Ref. [14] or Appendix A) the error probability $P_e(\psi)$ for

the TRP final state $|\psi_a\rangle = U_a|\psi\rangle$, relative to the target final state $|\psi_{tgt}\rangle = U_{tgt}|\psi\rangle$. The gate error probability P_e is defined to be the worst-case value [31] of $P_e(\psi)$: $P_e \equiv \max_{|\psi\rangle} P_e(\psi)$. Introducing the positive operator $P = \left(U_a^\dagger - U_{tgt}^\dagger\right)(U_a - U_{tgt})$, Ref. [14] showed that the error probability P_e satisfies the upper bound $P_e \leq Tr\, P$. Once U_a is known, $Tr\, P$ is easily evaluated, and so it is a convenient proxy for P_e which is harder to calculate. $Tr\, P$ also has the virtue of being directly related to the gate fidelity $\mathcal{F}_n = (1/2^n)\ Re\left[\, Tr\left(U_a^\dagger U_{tgt}\right)\right]$, where n is the number of qubits acted on by the gate. It is straightforward to show [15] that $\mathcal{F}_n = 1 - \left(1/2^{n+1}\right) Tr\, P$. The simulations calculate $Tr\, P$, which is then used to upper bound the gate error probability P_e. Note that minimizing $Tr\, P$ is equivalent to maximizing the gate fidelity $\mathcal{F}_n$.

The procedure for solving the EL equations for optimal control was briefly described in Section II D. The one-qubit TRP gates presented in Ref. [17] and the two-qubit TRP gate presented in Ref. [15] will serve as the good gates that are to be improved. For the reader's convenience, the TRP sweep parameters for these gates are presented in Appendix A 3, along with their associated gate error probabilities and fidelities. For a particular target gate U_{tgt} belonging to $\mathcal{G}_U$ (see Section III A 2), the TRP sweep parameters corresponding to U_{tgt} determine the TRP control field $\mathbf{F}_0(\tau)$ which then drives the nominal Hamiltonian $H_0(\tau)$ (see Eqs. (45) and (46) for one- and two-qubit gates, respectively). The nominal Hamiltonian in turn produces the initial good approximate gate $U_0(\tau_0/2, -\tau_0/2)$ that is to be improved. Here τ is the dimensionless time introduced above, and $\tau_0 \equiv aT/b$. For each gate in $\mathcal{G}_U$, its TRP approximation $U_0(\tau_0/2, -\tau_0/2)$ is also reproduced in Appendix A 3. For the two strategies introduced in Section II D, the numerical simulation implements the following procedure:

1. For both Strategies, integrate the Schrodinger equation with the nominal Hamiltonian $H_0(\tau)$ to obtain $U_0(\tau_0/2, -\tau_0/2)$; calculate $\Delta\boldsymbol{\beta}$. For Strategy 1, also calculate $\mathbf{w}$.

2. For both Strategies, calculate $\overline{G}_j(\tau) = U_0^\dagger(\tau)\mathcal{G}_j U_0(\tau)$, where we have abbreviated $U_0(\tau, -\tau_0/2)$ as $U_0(\tau)$, and $\mathcal{G}_j(\tau) = \delta H/\delta F_j|_{\mathbf{F}_0(\tau)}$; form $G(\tau)$. For Strategy 1, skip Step 3, go to Step 4.

3. For Strategy 2, set $R(\tau) = I_{3\times 3}$ and $S(\tau) = I_{16\times 16}$, where $I_{n\times n}$ is the $n\times n$ identity matrix. The Ricatti equation then requires $Q(\tau) = G(\tau)G^\dagger(\tau)$. The resulting control gain matrix is $C(\tau) = G^\dagger(\tau)$.

4. (a) For Strategy 1, use Eq. (25) to determine the control modification $\Delta\mathbf{F}(\tau)$.

   (b) For Strategy 2, solve Eq. (41) with initial condition Eq. (22) for $\Delta\mathbf{y}(\tau)$; substitute $\Delta\mathbf{y}(\tau)$ and $C(t)$ into the feedback control law (Eq. (37)) to determine $\Delta\mathbf{F}(\tau)$.

5. For both Strategies, with the improved control field $\mathbf{F}(\tau) = \mathbf{F}_0(\tau) + \Delta\mathbf{F}(\tau)$, numerically integrate the Schrodinger equation to determine the new propagator $U(\tau, -\tau_0/2)$, and the improved gate $U(\tau_0/2, -\tau_0/2)$.

6. For both Strategies, calculate $Tr\, P$ for the new gate. This gives: (i) an upper bound on the new gate error probability $P_e \leq Tr\, P$, and (ii) the new gate fidelity $\mathcal{F} = 1 - (1/2^{n+1}) Tr\, P$.

B. Ideal Control

Here we illustrate the use of neighboring optimal control to improve the performance of a good quantum gate. To avoid obscuring the presentation by showing results for all gates in $\mathcal{G}_U$, we instead focus in the remainder of this section on the one-qubit Hadamard gate. The results for the remaining gates in $\mathcal{G}_U$ appear in Appendix D. In this subsection we examine performance improvements under ideal control, while Section III C considers the robustness of these improvements to some important control imperfections.

1. *Performance improvement*

As noted in Section II D, we use: (i) Strategy 1 to determine the performance improvements for the one-qubit gates in $\mathcal{G}_U$; and (ii) Strategy 2 for the two-qubit controlled-phase gate. We saw there that Strategy 1 produces a one-qubit gate satisfying $U(\tau_0/2) = U_{tgt} + \mathcal{O}(\Delta^2)$. Here we use the numerical simulation procedure described in Section III A 3 to determine the small residual error in a one-qubit gate $U(\tau_0/2)$. A comparable discussion for the two-qubit modified controlled-phase gate appears in Appendix D. Thus, for a given one-qubit TRP gate, we use the corresponding values of λ and η_4 appearing in Table VII to determine the nominal control field $\mathbf{F}_0(\tau)$. This determines the nominal Hamiltonian $H_0(\tau) = -\boldsymbol{\sigma}\cdot\mathbf{F}_0(\tau)$, and numerical integration of the Schrodinger equation (see Eq. (2)) determines the nominal state trajectory $U_0(\tau)$. Following the simulation protocol, $U_0(\tau)$ is used to determine $\delta\beta$ and $\mathbf{w}$, as well as the matrix $G(\tau)$. Eq. (25) is then used to determine the control modification $\Delta\mathbf{F}(\tau)$, and thus the improved control field $\mathbf{F}(\tau) = \mathbf{F}_0(\tau) + \Delta\mathbf{F}(\tau)$. The new Hamiltonian is $H(\tau) = -\boldsymbol{\sigma}\cdot\mathbf{F}(\tau)$, and numerical integration of the Schrodinger equation determines the improved state trajectory $U(\tau)$. The improved one-qubit gate is then $U(\tau_0/2)$. With the new gate in hand we determine $Tr\, P$ which then provides an upper bound on the gate error probability $P_e \leq Tr\, P$. If so desired, one can also calculate the gate fidelity $\mathcal{F} = 1 - (1/4) Tr\, P$.

As noted earlier, we focus our remarks in the remainder of this Section on the Hadamard gate. A comparable discussion of the other gates in $\mathcal{G}_U$ appears in Ap-

pendix D. Implementing the above numerical simulation protocol using the TRP approximation to the Hadamard gate as the starting point returns an improved gate with $Tr\,P = 1.04\times10^{-8}$, and thus a gate error probability satisfying $P_e \leq 1.04\times10^{-8}$. We see that use of neighboring optimal control has produced a *four order-of-magntiude* reduction in the gate error probability compared to the starting TRP gate for which $P_e \leq 1.12\times10^{-4}$. The error probability for the improved gate is also *four orders-of-magnitude* less than the target accuracy threshold of 10^{-4}. Because P_e is so small, we do not write out the unitary matrix produced by the numerical simulation as it agrees with the target Hadamard unitary matrix to 6 significant figures. For completeness, Table I gives the $Tr\,P$ upper bound on the gate error probability P_e for all gates in $\mathcal{G}_U$, with and without the neighboring optimal control improvements. We see that neighboring optimal control reduces the gate error probability by: (i) four orders-of-magnitude for all one-qubit gates in $\mathcal{G}_U$; and (ii) two orders-of-magnitude for the two-qubit modified controlled-phase gate. We examine the robustness of these performance gains to some important control imperfections in Section III C. Before moving on to that discussion, we examine in the following subsection, the amount of bandwidth needed to realize the control modification $\mathbf{F}(\tau)$.

2. *Control field bandwidth*

We now examine the bandwidth required to realize the control modifications $\Delta\mathbf{F}(t)$. We explicitly consider the Hadamard gate in this subsection; a similar analysis for the remaining target gates in $\mathcal{G}_U$ appears in Appendix D. To provide context for our results, we note that arbitrary waveform generators (AWG) are commercially available with bandwidths as large as 5 GHz [32].

For a one-qubit target gate, the control modification $\Delta\mathbf{F}(t)$ is given by Eq. (25), with $G(t)$ and $\mathbf{w}$ determined by the numerical simulation protocol described in Sections III A 3 and III B 1. Figure 1 shows the x-component of the control field modification $\Delta F_x(\tau)$ as a function of the dimensionless time τ for the Hadamard gate as target. Figure 2 shows its Fourier transform $\Delta\mathcal{F}_x(\omega)$. We estimate the (dimensionless) bandwidth of $\Delta\mathcal{F}_x(\omega)$ by determining the frequency $\omega_{0.1}$ at which $\Delta\mathcal{F}_x(\omega_{0.1})$ is 10% of the peak value $\Delta\mathcal{F}_x(0)$. Examination of the numerical data used to produce Figure 2 gives $\omega_{0.1} = 4.0$. To convert this into a dimensionful bandwidth we suppose that the inversion time $T = 1\,\mu$s. This corresponds to a dimensionless inversion time of $\tau_0 = 160$ for the one-qubit gates so that the dimensionful bandwidth $\overline{\omega}_{0.1}$ is related to the dimensionless bandwidth $\omega_{0.1}$ by:

$$\frac{\overline{\omega}_{0.1}}{\omega_{0.1}} = \frac{160}{1\mu\text{s}} = 160\,\text{MHz}. \tag{47}$$

Thus the bandwidth needed to implement the control modification $\Delta\mathbf{F}(t)$ for the Hadamard gate is $\overline{\omega}_{0.1} =$ (160MHz)(4.0) = 640MHz. This is well within the range of commercially available AWGs. Table II lists the bandwidth required to implement the control modification for each of the target gates in $\mathcal{G}_U$. The analysis for the other one-qubit gates is similar to that of the Hadamard gate, while that of the two-qubit modified controlled-phase gate has only minor differences. The analysis of these other gates appears in Appendix D. We see that the bandwidth required to implement the neighboring optimal control performance improvements for all gates

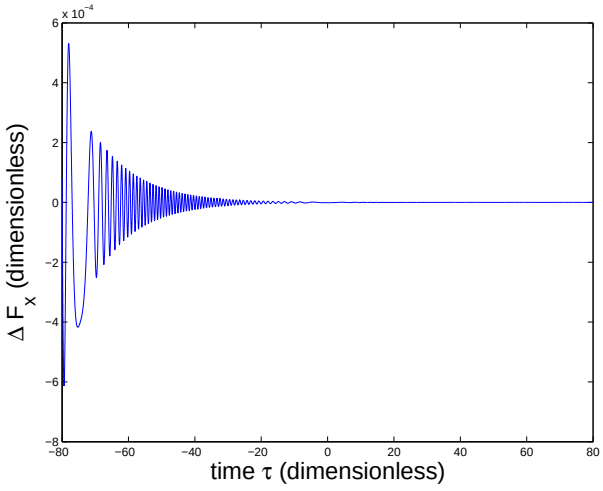

FIG. 1: (Color online) The control modification x-component $\Delta F_x(\tau)$ used to implement a neighboring optimal control improved approximation to the Hadamard gate. Here τ is dimensionless time.

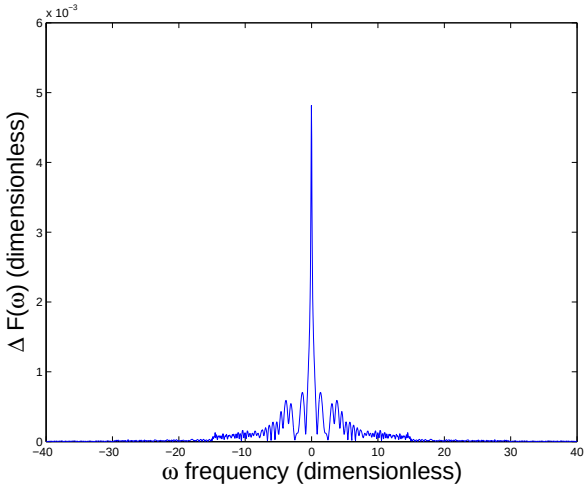

FIG. 2: (Color online) The Fourier transform $\Delta\mathcal{F}_x(\omega)$ of $\Delta F_x(\tau)$ for the Hadamard Gate as target. Here ω is dimensionless frequency.

TABLE I: Simulation results for all target gates in the universal set $\mathcal{G}_U$ for ideal control. The first column lists the target quantum gates, while the second column lists the $Tr\,P$ upper bound for the gate error probability P_e for gates whose performance is improved using neighboring optimal control (NOC). The third column lists the $Tr\,P$ upper bound for the starting TRP gates which do not use NOC. We see that NOC has reduced the error probability for all one-qubit gates by *four orders-of-magnitude*, and by *two orders-of-magnitude* for the two-qubit controlled-phase gate. The robustness of these reductions to control imperfections is examined in Section III C. Although not included in the Table, the gate fidelity $\mathcal{F}_n$ for an n-qubit gate can be determined from $Tr\,P$ using $\mathcal{F}_n = 1 - (1/2^{n+1})Tr\,P$.

Target Gate	$P_e \leq TrP$ (with NOC)	$P_e \leq TrP$ (without NOC)
NOT	$\leq 8.58 \times 10^{-9}$	$\leq 6.27 \times 10^{-5}$
Hadamard	$\leq 1.04 \times 10^{-8}$	$\leq 1.12 \times 10^{-4}$
Modified $\pi/8$	$\leq 1.06 \times 10^{-8}$	$\leq 2.13 \times 10^{-4}$
Modified phase	$\leq 1.08 \times 10^{-8}$	$\leq 4.62 \times 10^{-4}$
Modified controlled-phase	$\leq 5.21 \times 10^{-5}$	$\leq 1.27 \times 10^{-3}$

TABLE II: Bandwidth requirements for neighboring optimal control improved quantum gates. The dimensionful values assume a one-qubit (two-qubit) gate time of 1μs (5μs). Note that the bandwidth for the nominal TRP control field $\mathbf{F}_0(t)$ is less than 1% of the bandwidth of the control modification $\Delta\mathbf{F}(t)$. We thus use the bandwidth for $\Delta\mathbf{F}(t)$ as the total bandwidth. Column 1 lists the target gate; column 2 the dimensionless bandwidth $\omega_{0.1}$; while column 3 gives the dimensionful bandwidth $\overline{\omega}_{0.1}$.

Target Gate	$\omega_{0.1}$ (dimensionless)	$\overline{\omega}_{0.1}$ (MHz)
NOT	0.80	130
Modified $\pi/8$	1.3	210
Modified phase	1.9	300
Hadamard	4.0	640
Modified controlled-phase	34	820

in $\mathcal{G}_U$ is squarely within the range of existing commercially available AWGs. Note that Eq. (47) indicates that the dimensionful bandwidth $\overline{\omega}_{0.1}$ scales as $1/T$ in the inversion time T. Thus, if desired, one can always reduce the bandwidth of the control modification $\Delta\mathbf{F}(t)$ by increasing the inversion time (viz. gate time) T.

C. Robustness to control imperfections

In this subsection we examine the robustness of the neighboring optimal control (NOC) performance gains found in Section III B 1 to two important control imperfections. In the interests of clarity, we again focus on the Hadamard gate here, and present a similar analysis for the other gates in $\mathcal{G}_U$ in Appendix D. In Section III C 1 we examine the impact of control parameters with finite precision; while in Section III C 2 we consider phase noise in the nominal control field.

1. *Finite-precision control parameters*

The NOC formalism introduced in this paper requires an input state trajectory $U_0(\tau)$ that yields a good approximation to a target gate U_{tgt}. The control modification $\Delta\mathbf{F}(\tau)$ determined by the formalism is optimum for $U_0(\tau)$, or equivalently, for the nominal control $\mathbf{F}_0(\tau)$. Alteration of the nominal control field $\mathbf{F}_0(\tau) \rightarrow \mathbf{F}'_0(\tau)$ alters the state trajectory $U_0(\tau) \rightarrow U'_0(\tau)$, with the result that the control modification $\Delta\mathbf{F}(\tau)$ may no longer be optimal for the altered trajectory $U'_0(\tau)$. Because the hardware used to produce $\mathbf{F}_0(\tau)$ has limited precision, it becomes important to determine the degree of precision to which the control parameters must be specified if the NOC performance gains are to survive the limitation of finite-precision control.

For the Hadamard gate, Table VII in Appendix D gives $\lambda = 7.820$ and $\eta_4 = 1.792 \times 10^{-4}$ as the TRP control parameters that produce a nominal control field $\mathbf{F}_0(\tau)$, and state trajectory $U_0(\tau)$, for which the gate error probability satisfies $P_e \leq 1.12 \times 10^{-4}$. For these control parameter values, NOC determines the control modification $\Delta\mathbf{F}(\tau)$ (see Section III B 1) which yields a new gate with $P_e \leq 1.04 \times 10^{-8}$. To examine the robustness of this performance improvement, we shift λ (η_4) away from its optimum value by 1 in its fourth significant digit, while keeping η_4 (λ) at optimum. This shift causes $\mathbf{F}_0(\tau) \rightarrow \mathbf{F}'_0(\tau)$. We then numerically simulate the Schrodinger dynamics driven by the Hamilto-

nian $H(\tau) = -\boldsymbol{\sigma} \cdot \mathbf{F}'(\tau)$, where the new control field $\mathbf{F}'(\tau) = \mathbf{F}'_0(\tau) + \Delta\mathbf{F}(\tau)$, and $\Delta\mathbf{F}(\tau)$ is the NOC modification that corresponds to the nominal control field $\mathbf{F}_0(\tau)$. Tables III (IV) show how the $Tr\,P$ upper bound for the

TABLE III: Sensitivity of TrP to a small variation of λ away from its optimum value for the one-qubit Hadamard gate. For all λ values, η_4 is maintained at its optimum value $\eta_4 = 1.792 \times 10^{-4}$. Column 2 (3) shows the variation of $Tr\,P$ when the control field includes (omits) the NOC control modification $\Delta\mathbf{F}(\tau)$.

λ	TrP (with NOC)	TrP (without NOC)
7.819	2.62×10^{-4}	8.15×10^{-4}
7.820	1.04×10^{-8}	1.12×10^{-4}
7.821	4.44×10^{-4}	2.07×10^{-3}

TABLE IV: Sensitivity of TrP to a small variation of η_4 away from its optimum value for the one-qubit Hadamard gate. For all η_4 values, λ is maintained at its optimum value $\lambda = 7.820$. Column 2 (3) shows the variation of $Tr\,P$ when the control field includes (omits) the NOC control modification $\Delta\mathbf{F}(\tau)$.

η_4	TrP (with NOC)	TrP (without NOC)
1.791×10^{-4}	5.75×10^{-3}	2.86×10^{-2}
1.792×10^{-4}	1.04×10^{-8}	1.12×10^{-4}
1.793×10^{-4}	7.76×10^{-3}	3.11×10^{-2}

gate error probability P_e changes due to a small shift in λ (η_4) away from its optimum value. For comparison, we also show how $Tr\,P$ changes when the new control field does not contain the NOC modification: $\mathbf{F}'(\tau) = \mathbf{F}'_0(\tau)$. It is clear from these Tables that both λ and η_4 must be controllable to better than one part in $10,000$ if the NOC performance gains are to be realized. Such control parameter precision is attainable using an AWG with 14-bit vertical resolution (viz. one part in $2^{14} = 16,384$). Such AWGs are available commercially [33]. Note that 13-bit precision corresponds to a precision of one part in $2^{13} = 8192$, and so to an uncertainty in the fourth significant digit. Thus with less than 14-bits of precision, Tables III and IV indicate that the NOC performance gains will be washed out by the uncertainty in the least significant digit of λ and η_4. Lastly, notice that the NOC improved Hadamard gate outperforms the unimproved nominal TRP gate, even in the presence of finite precision control parameters. This is true for the other gates in $\mathcal{G}_U$ as well.

2. *Phase/timing jitter*

Phase jitter arises from timing errors in the clock used by an AWG to produce a desired control signal. Ideally, the clock outputs a sequence of "ticks" with constant time separation T_{clock}, derived from an oscillation with phase $\phi(t) = 2\pi f_{clock} t$ and frequency $f_{clock} = 1/T_{clock}$. A real clock only approximates this ideal behavior. In actuality, the time T between ticks is a stochastic process $T = T_{clock} + \delta t$, where the stochastic timing error δt has: (i) vanishing time-average $\overline{\delta t} = 0$; and (ii) a standard deviation $\sigma_t = \sqrt{\overline{\delta t^2}}$ which quantifies the spread of the tick intervals about T_{clock}. The spread σ_t is known as timing jitter. The timing error δt gives rise to a phase error $\delta\phi = (2\pi f_{clock})\delta t$ which has: (i) zero time-average $\overline{\delta\phi} = 0$; and (ii) standard deviation $\sigma_\phi = \sqrt{\overline{\delta\phi^2}}$ which characterizes the spread about 2π of the phase accumulated between ticks: $\phi = 2\pi f_{clock} T$. The spread σ_ϕ is known as phase jitter. As σ_ϕ and σ_t are two ways of describing the clock timing error, the ratio of spread to period for the phase ($\sigma_\phi/2\pi$) and the time (σ_t/T_{clock}) are the same. Equating them, and solving for σ_t gives

$$\sigma_t = \frac{\sigma_\phi}{2\pi f_{clock}}. \tag{48}$$

This expression can be thought of as a change in units from jitter in radians (viz. σ_ϕ) to jitter in seconds (viz. σ_t).

Phase jitter is anticipated to affect the performance of the TRP gates used in our illustration of the NOC formalism. We saw in Section III A 1 that the performance of these gates relies on quantum interference effects that arise during a TRP sweep. In the presence of phase jitter, the TRP twist profile $\phi_4(\tau) = (\eta_4/2\lambda)\tau^4$ develops phase noise $\delta\phi(\tau)$ due to the timing error $\delta\tau$ in τ. For sufficiently strong phase jitter, this phase noise is expected to wash out the interference effects that underlie the good performance of the TRP gates. Specifically, since this noise adds to the TRP twist phase $\phi_4(\tau) \to \phi'_4(\tau) = \phi_4(\tau) + \delta\phi(\tau)$, it causes the (dimensionless) TRP control field $\mathbf{F}'_0(\tau) = (1/\lambda)\left[\cos\phi'_4(\tau)\hat{\mathbf{x}} + \sin\phi'_4(\tau)\hat{\mathbf{y}} + \tau\hat{\mathbf{z}}\right]$ to twist incorrectly. The control field with the NOC modification is now $\mathbf{F}'(\tau) = \mathbf{F}'_0(\tau) + \Delta\mathbf{F}(\tau)$, where $\Delta\mathbf{F}(\tau)$ is the neighboring optimal control modification determined for the TRP control $\mathbf{F}_0(\tau)$ with *jitter-free* twist phase $\phi_4(\tau)$. It is important to appreciate that the phase noise $\delta\phi(\tau)$ is unpredictable and so it is not realistic to assume that we can recalculate the control modification $\Delta\mathbf{F}(\tau)$ so that it is optimal for $\mathbf{F}'_0(\tau)$ since $\mathbf{F}'_0(\tau)$ is not known until the gate is applied. Thus, for a given target gate, one can only calculate the control modification $\Delta\mathbf{F}(\tau)$ which is optimal for the jitter-free TRP control $\mathbf{F}_0(\tau)$, and add it to the noisy TRP control $\mathbf{F}'_0(\tau)$. Since $\Delta\mathbf{F}(\tau)$ is not optimal for $\mathbf{F}'(\tau)$, the NOC performance improvements are expected to be reduced by phase jitter.

To quantitatively study the effects of phase/timing jitter on the NOC performance gains, we modelled the phase noise $\delta\phi(\tau)$ as shot noise and used the model to generate numerical realizations of the phase noise $\delta\phi(\tau)$. The details of the model and the protocol used to generate noise realizations is described in Appendix C. For

each noise realization, we determined the state trajectory $U(\tau)$ by numerically simulating the Schrodinger dynamics generated by the noisy control field $\mathbf{F}'(\tau)$, and used it to determine the $Tr\,P$ upper bound for the gate error probability P_e. For each target gate U_{tgt} and given value of phase jitter σ_ϕ (equivalently, mean phase noise power $\overline{P}$, see below), we generated ten realizations of phase noise $\delta\phi(\tau)$, and determined the ten corresponding values of $Tr\,P$. The average $\langle Tr\,P\rangle$ and standard deviation $\sigma(Tr\,P)$ for these values was calculated and used to approximate the noise-averaged NOC gate performance: $P_e \leq \langle Tr\,P\rangle \pm \sigma(Tr\,P)$. We carried out simulations for various values of σ_ϕ, and present our results for the Hadamard gate in Figure 3.

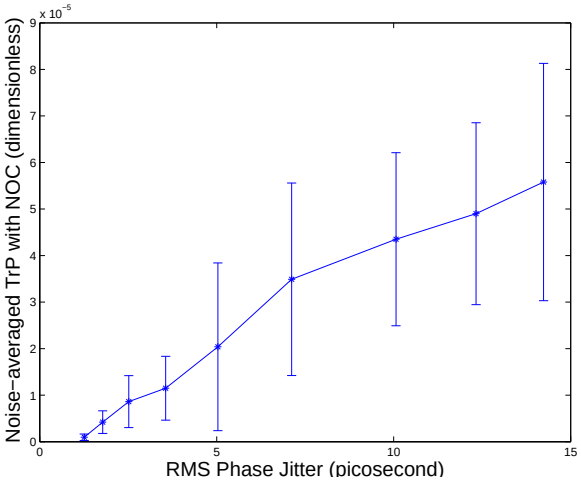

FIG. 3: (Color online) The noise-averaged value of TrP with NOC versus timing jitter $\sigma_t = \sigma_\phi/(2\pi f_{clock})$ for the Hadamard gate. For each σ_t, ten realizations of phase noise were generated, and for each realization, gate performance was determined by numerical simulation of the Schrodinger dynamics generated by the control field $\mathbf{F}'(\tau)$ that includes the noisy TRP nominal control $\mathbf{F}'_0(\tau)$ and the NOC modification $\Delta\mathbf{F}(\tau)$ (see text). The average and standard deviation were determined for the resulting ten $Tr\,P$ values. For each value of σ_t, the average of $Tr\,P$ is plotted, and the standard deviation is used to specify the error bar. To obtain σ_t, we have assumed that $f_{clock} = 1$GHz (see text).

To put Figure 3 into context, we note that AWGs with timing jitter $\sigma_t = 5$ps and clock frequency $f_{clock} = 1$GHz are commercially available [34]. In Appendix C we show that the phase noise variance $\overline{\delta\phi^2}$ is equal to the mean phase noise power $\overline{P}$. Since $\sigma_\phi = \sqrt{\overline{\delta\phi^2}}$, we have that $\sigma_\phi = \sqrt{\overline{P}}$, and so phase jitter is simply an alternative way to represent phase noise power. Eq. (48) is then used to convert phase jitter σ_ϕ into timing jitter σ_t. The horizontal axis in Figure 3 is thus simply an encoding of phase noise power. The largest phase noise power value used in the simulations was $\overline{P} = 0.008$, which gives

$$\sigma_t = \frac{\sqrt{0.008}}{2\pi(10^9\,\mathrm{s}^{-1})} = 14.2\mathrm{ps}.$$

This corresponds to the right-most data-point in Figure 3. A similar conversion of phase noise power was done for the other simulation data-points. At $\sigma_t = 5.03$ps, appropriate for commercially available AWGs, Figure 3 indicates that $P_e \leq (2.04 \pm 1.80) \times 10^{-5}$. From Table I, we see that, for ideal control, NOC produced a Hadamard gate with $P_e \leq 1.04 \times 10^{-8}$. As anticipated, the NOC performance gains are impacted by phase jitter. Figure 3 also shows that if an AWG was available with $\sigma_t = 1.26$ps, then $P_e \leq (9.59 \pm 6.94) \times 10^{-7}$, which is: (i) an order of magnitude reduction in the impact of phase jitter compared to $\sigma_t = 5.03$ps; and (ii) *two orders-of-magnitude* less than the target accuracy threshold of 10^{-4}, underscoring the importance of reducing timing jitter in the control electronics. We discuss this further below.

In Table V we display the impact of phase/timing jitter on the NOC performance gains of all gates in $\mathcal{G}_U$ for timing jitter $\sigma_t = 5.03$ps. We see that, even with timing jitter at the level found in commercially available AWGs, all gates in $\mathcal{G}_U$ have gate error probabilities that are an *order of magnitude smaller* than the target accuracy threshold value of 10^{-4}. Notice also the insensitivity of the two-qubit TRP gate to 5.03ps timing jitter. The standard deviation for this gate, $\sigma(TrP) = 5.26 \times 10^{-11}$, is displayed as zero to three significant figures in Table V.This weak sensitivity to timing jitter is not completely surprising given the weak sensitivity of this gate to imprecision in λ and η_4 that was found in Ref. [15], and thus to imprecision in the twisting of the control field. The critical parameters for this gate are d_1, d_4, and c_4 (see Appendix D 2 a).

In Table VI we display the impact of phase/timing jitter on the NOC performance gains of all gates in $\mathcal{G}_U$ for timing jitter $\sigma_t = 1.26$ps. We see that the gate error probability for the one-qubit gates is reduced by an order-of-magnitude ($P_e \sim 10^{-5} \to 10^{-6}$) compared to the error probability at $\sigma_t = 5.03$ps. The two-qubit gate error probability is unchanged at $P_e = 5.21 \times 10^{-5}$, although its standard deviation is now $\sigma(TrP) = 4.24 \times 10^{-14}$. Thus reducing timing jitter by a factor of 5 produces one-qubit gates whose error probability is *two orders-of-magnitude* smaller than the target accuracy threshold of 10^{-4}. For a threshold $P_a \sim 10^{-3}$ appropriate for surface and color quantum error correcting codes, *all gates* in $\mathcal{G}_U$ operate 2–3 *orders-of-magnitude* below threshold at $\sigma_t = 1.26$ps. Thus, for AWGs operating at this reduced level of timing jitter, the impact of phase/timing jitter on the NOC performance gains is greatly mitigated.

Lastly, note that for starting gates whose good performance is not due to quantum interference, phase jitter may have less impact on the NOC performance gains than for the TRP gates examined here.

TABLE V: Sensitivity of TrP to timing jitter $\sigma_t = \sqrt{\bar{P}}/(2\pi f_{clock})$ for all target gates in the universal set $\mathcal{G}_U$. For all gates, the numerical simulations used mean noise power $\bar{P} = 0.001$, which corresponds to timing jitter $\sigma_t = 5.03$ps for $f_{clock} = 1$GHz. For each gate, ten phase noise realizations were generated (see Appendix C), leading to ten values of the $Tr\,P$ upper bound on the gate error probability $P_e \leq Tr\,P$. The third column lists, for each gate, the corresponding average $< TrP >$, and uses the standard deviation $\sigma(TrP)$ to indicate the spread of $Tr\,P$ about the average.

Gate	Timing-jitter σ_t	$P_e \leq < TrP > \pm\sigma$(TrP) with NOC
Hadamard	$5.03ps$	$(2.04 \pm 1.80) \times 10^{-5}$
NOT	$5.03ps$	$(2.11 \pm 1.64) \times 10^{-5}$
Modified $\pi/8$	$5.03ps$	$(2.92 \pm 1.96) \times 10^{-5}$
Modified phase	$5.03ps$	$(3.04 \pm 2.16) \times 10^{-5}$
Modified controlled phase	$5.03ps$	$(5.21 \pm 0.00) \times 10^{-5}$

TABLE VI: Sensitivity of TrP to timing jitter $\sigma_t = \sqrt{\bar{P}}/(2\pi f_{clock})$ for all target gates in the universal set $\mathcal{G}_U$. For all gates, the numerical simulations used mean noise power $\bar{P} = 6.25 \times 10^{-5}$, which corresponds to timing jitter $\sigma_t = 1.26$ps for $f_{clock} = 1$GHz. For each gate, ten phase noise realizations were generated (see Appendix C), leading to ten values of the $Tr\,P$ upper bound on the gate error probability $P_e \leq Tr\,P$. The third column lists, for each gate, the corresponding average $< TrP >$, and uses the standard deviation $\sigma(TrP)$ to indicate the spread of $Tr\,P$ about the average.

Gate	Timing-jitter σ_t	$P_e \leq < TrP > \pm\sigma$(TrP) with NOC
Hadamard	$1.26ps$	$(9.59 \pm 6.94) \times 10^{-7}$
Modified $\pi/8$	$1.26ps$	$(1.24 \pm 1.04) \times 10^{-6}$
NOT	$1.26ps$	$(1.82 \pm 1.14) \times 10^{-6}$
Modified phase	$1.26ps$	$(1.92 \pm 1.57) \times 10^{-6}$
Modified controlled phase	$1.26ps$	$(5.21 \pm 0.00) \times 10^{-5}$

IV. SUMMARY

In this paper we have shown how neighboring optimal control (NOC) theory can be used to improve the performance of a good quantum gate. We illustrated the NOC theoretical framework by using it to improve the performance of all gates in a universal set of quantum gates produced using a type of non-adiabatic rapid passage that has been studied in the literature [10–17]. We stress that the NOC approach introduced here is not limited to this family of starting gates—any other good quantum gate, or set of gates, could serve as input for the method. For ideal control (see Table I), the improvements are substantial : (i) for all one-qubit gates in the universal set, the gate error probabilities were reduced by *four orders-of-magnitude* ($10^{-4} \rightarrow 10^{-8}$); and (ii) for the two-qubit gate in the set, by *two orders-of-magnitude* ($10^{-3} \rightarrow 10^{-5}$). We examined the bandwidth required to implement the ideal controls and showed that for gate times $1\mu\text{s} \leq T \leq 5\mu\text{s}$, the bandwidth Δf for all gates was in the range $130\text{MHz} \leq \Delta f \leq 820\text{MHz}$, which is well within the capabilities of commercially available arbitrary waveform generators. We examined the robustness of these performance improvements to two important sources of non-ideal control: (i) control parameters with finite precision; and (ii) timing/phase jitter resulting for clock errors in the control electronics. We showed (see Section III C 1 and Appendix D 2 a) that the NOC performance gains require arbitrary waveform generators with 14-bit (17-bit) vertical resolution for the one-qubit (two-qubit) gates. We also showed (see Section III C 2 and Appendix D 2 b) that timing/phase jitter can significantly impact the NOC performance gains. We showed that for 5ps timing jitter (comparable to that in commerically available AWGs), the gate error probability satisfies $P_e \sim 10^{-5}$ for all the gates in the universal set, an order-of-magnitude lower than the accuracy threshold target value of 10^{-4}. Finally, we showed (Section III C 2) that if timing jitter can be reduced to $\sigma_t = 1.26$ps, the error probability for all one-qubit gates in $\mathcal{G}_U$ drops to $P_e \sim 10^{-6}$, while the two-qubit gate error probability remains unchanged at 5.21×10^{-5}. All gates thus operate with an error probability 1–2 *orders-of-magnitude* below the target threshold of 10^{-4}. Although we have focused on a target accuracy threshold $P_a = 10^{-4}$ throughout this paper, we note that for surface and color quantum error correcting codes, the accuracy threshold satisfies $P_a \sim 10^{-3}$ [18–22]. For these codes, the NOC improved gates *all* operate 2–3 *orders-of-magnitude* below threshold, even for non-ideal control. The availability of a universal set of quantum gates operating so far below threshold would have a significant impact on efforts to realize fault-tolerant quantum computing as it would greatly reduce the resources needed to implement such a com-

putation. It is hoped that the NOC gate performance improvements found in this paper might encourage an attempt to produce these high-fidelity gates experimentally.

We close by noting that we have assumed throughout this paper that the qubit longitudinal (T_1) and transverse (T_2) relaxation times are long compared to the gate operation time T_{gate}. This assumption is essential for any discussion of fault-tolerant quantum computing and error correction as it insures that the qubit state does not decohere away before the error-syndrome extraction circuit can be applied, and likely errors identified. When $T_1, T_2 \gg T_{gate}$, control imperfections may be anticipated to be the primary source of errors during a gate operation, and the qubit environment a secondary source. On the other hand, when $T_1, T_2 \lesssim T_{gate}$, the qubits are of sufficiently poor quality that errors from the qubit environment can be expected to be (at least) as bad as the types of errors we have examined in this paper. Our NOC strategy for improving a good quantum gate does not remove the need for high-quality qubits as the object of these gate operations.

Acknowledgments

We thank: C. Tahan for providing the computing resources used to obtain the simulation results reported in this paper; and F. Wellstood, V. Yakovenko, and R. Li for valuable discussions. F. G. thanks T. Howell III for continued support.

Appendix A: Twisted rapid passage - a few more necessary results

We illustrated the general theory developed in Section II by using it in Section III and Appendix D to improve the performance of a universal set of quantum gates implemented using a form of non-adiabatic rapid passage known as twisted rapid passage (TRP) [10]-[17]. In Section III A we provided a brief introduction to TRP. In this Appendix we complete our review of TRP. Appendix A 1 presents the derivation of the dimensionless one- and two-qubit Hamiltonians used to drive the quantum gates produced using TRP. Appendix A 2 derives an expression for the gate error probability, as well as a convenient upper bound for it. Finally, for the reader's convenience, Appendix A 3 collects previous results for the TRP sweep parameters, gate error probabilities and fidelities for the TRP-generated universal set of quantum gate studied in Refs. [15] and [17]. It also provides the TRP approximate gates $U_0(t = T)$ for each gate in $\mathcal{G}_U$. These gates serve as the good starting gates that are improved using neighboring optimal control. We stress that this approach to improving a good quantum gate (or set of gates) is not limited to this TRP-generated family of gates. Any good gate could provide the starting point for the method.

1. One- and two-qubit Hamiltonians

(a) For the one-qubit gates studied in this paper, the qubit is assumed to couple to an external control field $\mathbf{F}(t)$ through the Zeeman-interaction,

$$H_0^1(t) = -\boldsymbol{\sigma} \cdot \mathbf{F}(t), \tag{A1}$$

where $\mathbf{F}(t)$ has the TRP profile,

$$\mathbf{F}(t) = at\hat{\mathbf{z}} + b\cos\phi_4(t)\hat{\mathbf{x}} + b\sin\phi_4(t)\hat{\mathbf{y}}, \tag{A2}$$

and for quartic twist, $\phi_4(t) = (1/2)Bt^4$ with $-T/2 \leq t \leq T/2$. The Schrodinger equation for the propagator $U(t, -T/2)$ is

$$i\hbar\frac{dU(t)}{dt} = \left[-at\sigma_z - b\cos\phi_4(t)\sigma_x - b\sin\phi_4(t)\sigma_y\right]U(t), \tag{A3}$$

where we have suppressed the $-T/2$ dependence in $U(t, -T/2)$. It proves useful to express Eq. (A3) in dimensionless form. To that end we define: (i) the dimensionless time $\tau = (a/b)t$; (ii) the dimensionless inversion rate $\lambda = \hbar a/b^2$; and (iii) the dimensionless twist strength $\eta_4 = \hbar B b^2/a^3$. In terms of these parameters, Eq. (A3) becomes

$$i\frac{dU(\tau)}{d\tau} = H_0^1(\tau)U(\tau), \tag{A4}$$

where the dimensionless one-qubit Hamiltonian is

$$H_0^1(\tau) = \frac{1}{\lambda}\left[-\tau\sigma_z - \cos\phi_4(\tau)\sigma_x - \sin\phi_4(\tau)\sigma_y\right], \tag{A5}$$

and $\phi_4(\tau) = (\eta_4/2\lambda)\tau^4$. This is the nominal one-qubit Hamiltonian discussed in Section III A 3 that drives the numerical simulation of all one-qubit gates considered in this paper.

(b) Next we derive the dimensionless nominal two-qubit Hamiltonian $H_0^2(\tau)$ discussed in Section III A 3 and which drives the numerical simulations of the two-qubit modified controlled phase gate. Although a more general discussion is possible, it proves convenient to adopt the language of NMR which was the original experimental setting for TRP [11, 35].

The two-qubit Hamiltonian contains terms that Zeeman-couple each qubit to an external control field $\mathbf{F}(t)$, and an Ising interaction term that couples the two qubits. Note that alternative two-qubit interactions can easily be considered by straightforward modification of the following arguments. Our starting point is thus the Hamiltonian

$$\frac{\overline{H}_0^2(t)}{\hbar} = -\frac{1}{2}\sum_{i=1}^{2}\gamma_i\,\boldsymbol{\sigma}^i \cdot \mathbf{F}(t) - \frac{\pi}{2}\,J\,\sigma_z^1\sigma_z^2, \tag{A6}$$

where γ_i is the gyromagnetic ratio for qubit i, and J is the Ising interaction coupling constant. In the lab frame, $\mathbf{F}(t)$ has a static component $B_0\,\hat{\mathbf{z}}$ and a time-varying component $2B_{rf}\cos\phi_{rf}(t)\,\hat{\mathbf{x}}$. In the rotating wave approximation $\mathbf{F}(t)$ reduces to

$$\mathbf{F}(t) = B_0\,\hat{\mathbf{z}} + B_{rf}\cos\phi_{rf}(t)\,\hat{\mathbf{x}} - B_{rf}\sin\phi_{rf}(t)\,\hat{\mathbf{y}}. \quad \text{(A7)}$$

Introducing $\omega_i = \gamma_i B_0$ and $\omega_i^{rf} = \gamma_i B_{rf}$ $(i = 1, 2)$, and inserting Eq. (A7) into Eq. (A6) gives

$$\frac{\overline{H}^{\,2}_{\,0}(t)}{\hbar} = \sum_{i=1}^{2}\left[-\frac{\omega_i}{2}\sigma_z^i - \frac{\omega_i^{rf}}{2}\left\{\cos\phi_{rf}\sigma_x^i - \sin\phi_{rf}\sigma_y^i\right\}\right] - \frac{\pi}{2}\,J\,\sigma_z^1\sigma_z^2. \quad \text{(A8)}$$

Transformation to the detector frame is done via the unitary operator

$$U_{det}(t) = \exp\left[\,(i\phi_{det}(t)/2)\left(\sigma_z^1 + \sigma_z^2\right)\right].$$

The Hamiltonian in the detector frame is then [27]

$$\begin{aligned}\frac{\tilde{\mathrm{H}}_0^2(t)}{\hbar} &= U_{det}^{\dagger}\left(\frac{\overline{H}^{\,2}_{\,0}(t)}{\hbar}\right)U_{det} - iU_{det}^{\dagger}\frac{dU_{det}}{dt}\\ &= \sum_{i=1}^{2}\Big[\Big(-\frac{\omega_i}{2} + \dot{\phi}_{det}\Big)\sigma_z^i - \frac{\omega_i^{rf}}{2}\left\{\cos\left(\phi_{det} - \phi_{rf}\right)\sigma_x^i + \sin\left(\phi_{det} - \phi_{rf}\right)\sigma_y^i\right\}\Big] - \frac{\pi}{2}\,J\,\sigma_z^1\sigma_z^2. \end{aligned} \quad \text{(A9)}$$

As explained in Refs. [11, 35], to produce a TRP sweep in the detector frame it is necessary to sweep $\dot{\phi}_{det}$ and $\dot{\phi}_{rf}$ through a Larmor resonance frequency. We choose (somewhat arbitrarily) to sweep through the Larmor frequency ω_2:

$$\begin{aligned}\dot{\phi}_{det} &= \omega_2 + \frac{2at}{\hbar} + \Delta\\ \dot{\phi}_{rf} &= \dot{\phi}_{det} - \dot{\phi}_4. \end{aligned} \quad \text{(A10)}$$

Here $\phi_4(t) = (1/2)Bt^4$ is the twist profile for quartic TRP, and we have introduced a frequency shift parameter Δ whose value is determined by the sweep parameter optimization procedure described in Ref. [15]. Inserting Eqs. (A10) into Eq. (A9), and introducing $\delta\omega = \omega_1 - \omega_2$ and $b_i = \hbar\omega_i^{rf}/2$ $(i = 1, 2)$, we find

$$\frac{\tilde{\mathrm{H}}_0^2(t)}{\hbar} = \left[-\frac{(\delta\omega + \Delta)}{2} + \frac{at}{\hbar}\right]\sigma_z^1 + \left[-\frac{\Delta}{2} + \frac{at}{\hbar}\right]\sigma_z^2 - \frac{b_1}{\hbar}\left[\,\cos\phi_4\,\sigma_x^1 + \sin\phi_4\,\sigma_y^1\,\right] - \frac{b_2}{\hbar}\left[\,\cos\phi_4\,\sigma_x^2\sin\phi_4\,\sigma_y^2\,\right] - \frac{\pi}{2}\,J\,\sigma_z^1\sigma_z^2. \quad \text{(A11)}$$

We see that both qubits are acted on by a quartic TRP sweep in the detector frame. In keeping with our earlier choice of sweeping through the Larmor resonance of the second qubit, we use b_2 in the definitions of the dimensionless time τ, inversion rate λ, and twist strength η_4:

$$\begin{aligned}\tau &= \left(\frac{a}{b_2}\right)t \quad \text{(A12)}\\ \lambda &= \frac{\hbar a}{(b_2)^2} \quad \text{(A13)}\\ \eta_4 &= \left(\frac{\hbar B}{a^3}\right)(b_2)^2. \quad \text{(A14)}\end{aligned}$$

Since $\tilde{\mathrm{H}}_0^2(t)/\hbar$ has units of inverse-time, and b_2/a has units of time (Eq. (A12)), multiplying Eq. (A11) by b_2/a and using Eqs. (A12)–(A14) gives the dimensionless two-qubit Hamiltonian $\tilde{\mathrm{H}}_0^2(\tau)$:

$$\tilde{\mathrm{H}}_2(\tau) = \left[-\frac{(d_1 + d_2)}{2} + \frac{\tau}{\lambda}\right]\sigma_z^1 + \left[-\frac{d_2}{2} + \frac{\tau}{\lambda}\right]\sigma_z^2 - \frac{d_3}{\lambda}\left[\,\cos\phi_4\,\sigma_x^1 + \sin\phi_4\,\sigma_y^1\,\right] - \frac{1}{\lambda}\left[\,\cos\phi_4\,\sigma_x^2 + \sin\phi_4\,\sigma_y^2\,\right] - \frac{\pi}{2}\,d_4\,\sigma_z^1\sigma_z^2, \quad \text{(A15)}$$

where

$$\begin{aligned}d_1 &= \left(\frac{\delta\omega}{a}\right)b_2\\ d_2 &= \left(\frac{\Delta}{a}\right)b_2\\ d_3 &= \frac{b_1}{b_2}\\ d_4 &= \left(\frac{J}{a}\right)b_2. \end{aligned} \quad \text{(A16)}$$

As noted in Section III A 3, $\tilde{\mathrm{H}}_2(\tau)$ has a degeneracy in the resonance frequency of the energy level pairs $(E_1 \leftrightarrow E_2)$ and $(E_3 \leftrightarrow E_4)$. To break this degeneracy we add the term

$$\Delta H = c_4\,|E_4(\tau)\rangle\langle E_4(\tau)| \quad \text{(A17)}$$

to $\tilde{\mathrm{H}}_0^2(\tau)$, where $|E_4(\tau)\rangle$ is the instantaneous energy eigenstate of $\tilde{\mathrm{H}}_0^2(\tau)$ with eigenvalue $E_4(\tau)$. Our final Hamiltonian is then

$$H_0^2(\tau) = \tilde{\mathrm{H}}_0^2(\tau) + \Delta H \quad \text{(A18)}$$

which is the Hamiltonian given in Eq. (46). We see that $H_0^2(\tau)$ depends on the TRP sweep parameters $(\lambda,\ \eta_4)$, as well as on the parameters $(d_1, \ldots, d_4)$ and c_4. From Eq. (A16) we see that d_1, d_2, d_3, and d_4 are the dimensionless versions of, respectively, the Larmor frequency

difference $\delta\omega = \omega_1 - \omega_2$, the frequency shift parameter Δ, the ratio $b_1/b_2 = \gamma_1/\gamma_2$, and the Ising coupling constant J.

For a derivation of the one-qubit TRP Hamiltonian (Eq. (A1)) based on an NMR experimental implementation, see the Appendix of Ref. [10].

2. Gate error probability

The following argument is for an N-dimensional Hilbert space. As in Section III A 3, let U_a denote the actual unitary operation produced by a given set of TRP sweep parameters and U_{tgt} a target unitary operation we would like TRP to approximate as closely as possible. Introducing the operators $D = U_a - U_{tgt}$ and $P = D^\dagger D$, and the normalized state $|\psi\rangle$, we define $|\psi_a\rangle = U_a|\psi\rangle$ and $|\psi_{tgt}\rangle = U_{tgt}|\psi\rangle$. Now choose an orthonormal basis $|i\rangle$ $(i = 1, \ldots, N)$ such that $|1\rangle \equiv |\psi_{tgt}\rangle$ and define the state $|\xi_\psi\rangle$ via

$$|\psi_a\rangle = |\psi_{tgt}\rangle + |\xi_\psi\rangle \quad \text{(A19)}$$
$$= |1\rangle + |\xi_\psi\rangle \quad . \quad \text{(A20)}$$

Inserting $|\xi_\psi\rangle = \sum_{i=1}^N e_i|i\rangle$ into eq. (A20) gives

$$|\psi_a\rangle = (1 + e_1)\,|1\rangle + \sum_{i\neq 1} e_i|i\rangle \quad . \quad \text{(A21)}$$

Since $|\psi_{tgt}\rangle = |1\rangle$ is the target state, it is clear from Eq. (A21) that the error probability $P_e(\psi)$ for U_a (i. e. TRP) is

$$P_e(\psi) = \sum_{i\neq 1} |e_i|^2 \quad . \quad \text{(A22)}$$

We define the error probability P_e for the TRP gate to be

$$P_e \equiv \max_{|\psi\rangle} P_e(\psi) \quad . \quad \text{(A23)}$$

From Eq. (A19),

$$|\xi_\psi\rangle = D|\psi\rangle$$

and

$$\langle\xi_\psi|\xi_\psi\rangle = \langle\psi|D^\dagger D|\psi\rangle$$
$$= Tr\rho_\psi P \quad , \quad \text{(A24)}$$

where $\rho_\psi = |\psi\rangle\langle\psi|$. On the other hand,

$$\langle\xi_\psi|\xi_\psi\rangle = \sum_{i=1}^N |e_i|^2$$
$$= |e_1|^2 + P_e(\psi) \quad . \quad \text{(A25)}$$

Combining Eqs. (A24) and (A25) gives

$$P_e(\psi) = \langle\xi_\psi|\xi_\psi\rangle - |e_1|^2$$
$$\leq \langle\xi_\psi|\xi_\psi\rangle = Tr\rho_\psi P \quad .$$

Since $P = D^\dagger D$ is Hermitian it can be diagonalized: $P = O^\dagger d\, O$ and $d = diag(d_1, \ldots, d_N)$. Thus

$$P_e(\psi) \leq Tr\,\overline{\rho}_\psi d \quad ,$$

where $\overline{\rho}_\psi = O\rho_\psi O^\dagger$. Let $d_* = \max(d_1, \ldots, d_N)$, then direct evaluation of the trace gives

$$Tr\,\overline{\rho}_\psi d = \sum_{i=1}^N d_i \left(\overline{\rho}_\psi\right)_{ii}$$
$$\leq \sum_{i=1}^N d_* \left(\overline{\rho}_\psi\right)_{ii} = d_*\, Tr\,\overline{\rho}_\psi = d_* \quad ,$$

where we have used that $Tr\,\overline{\rho}_\psi = 1$. Thus $P_e(\psi) \leq d_*$ for *all* states $|\psi\rangle$. From Eq. (A23), it follows that

$$P_e \leq d_* \quad , \quad \text{(A26)}$$

so that the largest eigenvalue d_* of P is an upper bound for the gate error probability P_e. Finally, notice that $P = D^\dagger D$ is a positive operator so that $d_i \geq 0$ for $i = 1, \ldots, N$. Thus $d_* \leq Tr\,P$ and so

$$P_e \leq d_* \leq Tr\,P \quad . \quad \text{(A27)}$$

Although $Tr\,P$ need not be as tight an upper bound on P_e as d_*, it is much easier to calculate and so is more convenient than d_* for use in the numerical simulations carried out in this paper.

3. Nominal gates

The nominal quantum gates whose performance is to be improved through neighboring optimal control are the set of one-qubit gates examined in Ref. [17], and the two-qubit modified controlled phase gate studied in Ref. [15]. As these papers showed, these gates provide a good approximation to the universal quantum gate set $\mathcal{G}_U$ introduced in Section III A 2. For the reader's convenience we reproduce in this subsection the main results of these papers which, for each gate, include: (i) the control parameters used to produce the approximate gate; (ii) the $Tr\,P$ upper bound on its gate error probability P_e; and (iii) its gate fidelity $\mathcal{F}$. These results are collected in Tables VII and VIII below. We also include the TRP-generated unitary gate $U_0(\tau = \tau_0/2)$ for each quantum gate in $\mathcal{G}_U$.

One-qubit gates: As was shown in Section III A 3 and Appendix A 1, the parameters λ, η_4, and $\tau_0 = aT/b$ fix the TRP control field $\mathbf{F}_0(\tau)$ that implements a particular nominal one-qubit gate. In all our one-qubit simulations $\tau_0 = 160$ [36]. Table VII lists the one-qubit target gates, and for each gate, the TRP control parameters that produce a good approximation U_a to it. Column 3 gives the upper bound $Tr\,P$ on the gate error probability P_e, and column 4 gives the gate fidelity $\mathcal{F}$ (see

TABLE VII: The nominal one-qubit gates used in this paper are those studied in Ref. [17]. For the reader's convenience, for each gate, we tabulate the control parameter values and gate performance reported in that work. The TRP sweep parameter values listed for λ and η_4 were found using the downhill simplex optimization algorithm; the TrP upper bound on the gate error probability (see Eq. (A27)) was found using numerical simulation of the one-qubit Schrodinger dynamics; and the gate fidelity $\mathcal{F}$ follows from $Tr\,P$ (see Sec. III A 3). The dimensionless inversion time $\tau_0 = 160$.

Gate	λ	η_4	TrP	$\mathcal{F}$
NOT	6.965	2.189×10^{-4}	6.27×10^{-5}	0.99998
Hadamard	7.820	1.792×10^{-4}	1.12×10^{-4}	0.99997
Modified $\pi/8$	8.465	1.675×10^{-4}	2.13×10^{-4}	0.99995
Modified phase	8.073	1.666×10^{-4}	4.62×10^{-4}	0.99988

Section III A 3). Ref. [17] describes the optimization procedure used to determine the control parameter values appearing in the Table.

Finally, we include the unitary gates produced by the TRP sweep parameters listed in Table VII.

(1) For the NOT gate, the TRP-generated unitary is:

$$U_{NOT} = \begin{pmatrix} -0.0014 + 0.0000\,i & 1.0000 + 0.0054\,i \\ 1.0000 - 0.0054\,i & 0.0014 + 0.0000\,i \end{pmatrix}.$$

With $U_0(\tau = \tau_0/2) = U_{NOT}$ and $U_{tgt} = \sigma_x$, we find that

$$Tr\,\left[U_0^\dagger(\tau_0/2)U_{tgt}\right] = 2 + 3.2000 \times 10^{-5}.$$

Recall that $\delta\beta = i\left[U_0^\dagger(\tau_0/2)U_{tgt} - I\right]$. Using the max-norm $\|U\| = \max_{i,j}|U_{ij}|$, we can show that $\|\delta\beta\| = 0.0054$. This sets the scale for small quantities introduced in Section II: $\Delta = \|\delta\beta\|$. Thus $\Delta^2 = 2.92 \times 10^{-5}$, and so we see that

$$Tr\,\left[U_0^\dagger(\tau_0/2)U_{tgt}\right] = 2 + \mathcal{O}(\Delta^2).$$

(2) For the Hadamard gate, the TRP-generated unitary is:

$$U_H = \begin{pmatrix} 0.7112 + 0.0000\,i & 0.7030 - 0.0016\,i \\ 0.7030 + 0.0016\,i & -0.7112 + 0.0000\,i \end{pmatrix}.$$

With $U_0(\tau = \tau_0/2) = U_H$ and $U_{tgt} = (1/\sqrt{2})\,(\sigma_x + \sigma_z)$, we find that

$$Tr\,\left[U_0^\dagger(\tau_0/2)U_{tgt}\right] = 2 + 6.7615 \times 10^{-5}.$$

Here $\|\delta\beta\| = 0.0081$ and so $\Delta^2 = 6.561 \times 10^{-5}$. Thus we see that

$$Tr\,\left[U_0^\dagger(\tau_0/2)U_{tgt}\right] = 2 + \mathcal{O}(\Delta^2).$$

(3) For the modified $\pi/8$ gate, the TRP-generated unitary is:

$$V_{\pi/8} = \begin{pmatrix} -0.0061 + 0.0000\,i & 0.9204 + 0.3910\,i \\ 0.9204 - 0.3910\,i & 0.0061 + 0.0000\,i \end{pmatrix}.$$

With $U_0(\tau = \tau_0/2) = V_{\pi/8}$ and $U_{tgt} = \cos(\pi/8)\sigma_x - \sin(\pi/8)\sigma_y$, we find that

$$Tr\,\left[U_0^\dagger(\tau_0/2)U_{tgt}\right] = 2 + 1.2034 \times 10^{-4}.$$

Here $\|\delta\beta\| = 0.0091$ and so $\Delta^2 = 8.2810 \times 10^{-5}$. Thus we see that

$$Tr\,\left[U_0^\dagger(\tau_0/2)U_{tgt}\right] = 2 + \mathcal{O}(\Delta^2).$$

(4) For the modified phase gate, the TRP-generated unitary is:

$$V_p = \begin{pmatrix} 0.0051 + 0.0000\,i & 0.7171 + 0.6969\,i \\ 0.7171 - 0.6969\,i & -0.0051 + 0.0000\,i \end{pmatrix}.$$

With $U_0(\tau = \tau_0/2) = V_p$ and $U_{tgt} = (1/\sqrt{2})\,(\sigma_x - \sigma_y)$, we find that

$$Tr\,\left[U_0^\dagger(\tau_0/2)U_{tgt}\right] = 2 + 2.3131 \times 10^{-4}.$$

Here $\|\delta\beta\| = 0.0143$ and so $\Delta^2 = 2.0449 \times 10^{-4}$. Thus we see that

$$Tr\,\left[U_0^\dagger(\tau_0/2)U_{tgt}\right] = 2 + \mathcal{O}(\Delta^2).$$

Two-qubit gate: As seen in Appendix A 1, the two-qubit nominal Hamiltonian $H_0^2(\tau)$ used to produce a good approximation to the two-qubit modified controlled phase gate V_{cp} is specified by the TRP sweep parameters λ, η_4, and τ_0, as well as the parameters $d_1, \ldots, d_4$ and c_4. All two-qubit simulations used $\tau_0 = 120$. Table VIII lists the values for the remaining control parameters; the $Tr\,P$ upper bound on the gate error probability P_e; and the gate fidelity $\mathcal{F}$. Ref. [15] describes the optimization procedure used to determine the control parameter values appearing in the Table.

For the modified controlled-phase gate, the TRP-generated unitary is:

$$Re(V_{cp}) = \begin{pmatrix} 0.9998 & 0.0155 & 0.0041 & 0.0028 \\ -0.0154 & 0.9997 & -0.0003 & 0.0021 \\ 0.0042 & -0.0002 & -0.9999 & -0.0038 \\ -0.0026 & -0.0021 & -0.0037 & 0.9999 \end{pmatrix};$$

TABLE VIII: The nominal two-qubit gate used in this paper is the modified controlled phase gate V_{cp} studied in Ref. [15]. For the reader's convenience, we tabulate the control parameter values and gate performance reported in that work. The control parameter values listed for λ, η_4, $d_1, \ldots, d_4$, and c_4 were found using simulated annealing; the TrP upper bound on the gate error probability (see Eq. (A27)) was found using numerical simulation of the one-qubit Schrodinger dynamics; and the gate fidelity $\mathcal{F}$ follows from $Tr\,P$ (see Sec. III A 3). The dimensionless inversion time $\tau_0 = 120$.

λ	η_4	d_1	d_2	d_3	d_4	c_4	TrP	$\mathcal{F}$
5.1	2.4×10^{-4}	11.702	-2.6	-0.41	6.6650	5.0003	1.27×10^{-3}	0.99984

$$Im(V_{cp}) = \begin{pmatrix} 0.0052 & -0.0108 & -0.0031 & -0.0017 \\ -0.0109 & 0.0064 & -0.0084 & 0.0068 \\ 0.0030 & 0.0084 & 0.0060 & -0.0079 \\ -0.0018 & 0.0068 & 0.0079 & 0.0026 \end{pmatrix}.$$

Finally, it is worth noting that Ref. [16] improved the performance of the modified controlled phase gate presented in Ref. [15] by interleaving a dynamical decoupling pulse sequence with the TRP control field. Although this complicates the time-dependence of the control field, it leads to an order of magnitude reduction in $Tr\,P$ ($Tr\,P = 1.27 \times 10^{-3} \rightarrow 8.87 \times 10^{-5}$), and only requires control parameters with 14-bit precision, compared to the 17-bit precision required in Ref. [15]. The reader is referred to Ref. [16] for further details. Although this new procedure produces a more robust high fidelity gate, the price paid is a control field that is much more difficult to implement experimentally. For this reason, in this paper, we have used the modified controlled phase gate studied in Ref. [15] as our nominal two-qubit gate.

Appendix B: Derivation of Eq. (27)

In this Appendix we derive Eq. (27) which we re-write here for convenience:

$$\begin{aligned} \mathcal{I} &= \sum_{j=1}^{3} \overline{G}_j \left(G^\dagger \mathbf{w}\right)_j \\ &= \begin{pmatrix} w_1 - w_4 & 2w_3 \\ 2w_2 & w_1 - w_4 \end{pmatrix}, \end{aligned} \tag{B1}$$

where $\mathbf{w}$ is a constant vector introduced in Section II D. To avoid cluttering equations, we suppress the time dependence of all vectors and matrices throughout this Appendix. We begin in Appendix B 1 by introducing a number of definitions aimed at making the flow of the calculation of $\mathcal{I}$ clearer, and then move on to the calculation of $\mathcal{I}$ in Appendix B 2.

1. Preliminary definitions

Our derivation assumes the quantum system of interest is a single qubit whose dynamics is driven by the Zeeman Hamiltonian $H = -\boldsymbol{\sigma} \cdot \mathbf{F}$. Following the development in Section II A, for this Hamiltonian, $\mathcal{G}_j = -\sigma_j$, where the $1, 2, 3$ components of $\boldsymbol{\sigma}$ are the x, y, z Pauli matrices, respectively, and

$$\overline{G}_j = U_0^\dagger \mathcal{G}_j U_0 = -U_0^\dagger \sigma_j U_0,$$

with

$$U_0 = \begin{pmatrix} U_{11} & U_{12} \\ U_{21} & U_{22} \end{pmatrix} = \begin{pmatrix} | & | \\ \mathbf{c}_1 & \mathbf{c}_2 \\ | & | \end{pmatrix}.$$

It follows from the unitarity of U_0 that $\mathbf{c}_1$ and $\mathbf{c}_2$ form an orthonormal set: $\mathbf{c}_i^\dagger \mathbf{c}_j = \delta_{ij}$.

It proves useful to define the vector pairs $(\mathbf{e}_1, \mathbf{e}_2)$, $(\mathbf{f}_1, \mathbf{f}_2)$, and $(\mathbf{g}_1, \mathbf{g}_2)$ as follows:

$$\begin{aligned} \sigma_x U_0 &= \begin{pmatrix} | & | \\ \mathbf{e}_1 & \mathbf{e}_2 \\ | & | \end{pmatrix}; \\ \sigma_y U_0 &= \begin{pmatrix} | & | \\ \mathbf{f}_1 & \mathbf{f}_2 \\ | & | \end{pmatrix}; \\ \sigma_z U_0 &= \begin{pmatrix} | & | \\ \mathbf{g}_1 & \mathbf{g}_2 \\ | & | \end{pmatrix}. \end{aligned}$$

Then

$$\overline{G}_1 = -\begin{pmatrix} \mathbf{c}_1^\dagger \mathbf{e}_1 & \mathbf{c}_1^\dagger \mathbf{e}_2 \\ \mathbf{c}_2^\dagger \mathbf{e}_1 & \mathbf{c}_2^\dagger \mathbf{e}_2 \end{pmatrix} = \begin{pmatrix} | & | \\ \boldsymbol{\gamma}_{1;1} & \boldsymbol{\gamma}_{1;2} \\ | & | \end{pmatrix}; \tag{B2a}$$

$$\overline{G}_2 = -\begin{pmatrix} \mathbf{c}_1^\dagger \mathbf{f}_1 & \mathbf{c}_1^\dagger \mathbf{f}_2 \\ \mathbf{c}_2^\dagger \mathbf{f}_1 & \mathbf{c}_2^\dagger \mathbf{f}_2 \end{pmatrix} = \begin{pmatrix} | & | \\ \boldsymbol{\gamma}_{2;1} & \boldsymbol{\gamma}_{2;2} \\ | & | \end{pmatrix}; \tag{B2b}$$

$$\overline{G}_3 = -\begin{pmatrix} \mathbf{c}_1^\dagger \mathbf{g}_1 & \mathbf{c}_1^\dagger \mathbf{g}_2 \\ \mathbf{c}_2^\dagger \mathbf{g}_1 & \mathbf{c}_2^\dagger \mathbf{g}_2 \end{pmatrix} = \begin{pmatrix} | & | \\ \boldsymbol{\gamma}_{3;1} & \boldsymbol{\gamma}_{3;2} \\ | & | \end{pmatrix}, \tag{B2c}$$

which gives

$$\mathbf{G}_1 = \begin{pmatrix} \boldsymbol{\gamma}_{1;1} \\ \boldsymbol{\gamma}_{1;2} \end{pmatrix}; \mathbf{G}_2 = \begin{pmatrix} \boldsymbol{\gamma}_{2;1} \\ \boldsymbol{\gamma}_{2;2} \end{pmatrix}; \mathbf{G}_3 = \begin{pmatrix} \boldsymbol{\gamma}_{3;1} \\ \boldsymbol{\gamma}_{3;2} \end{pmatrix},$$

and

$$G = \begin{pmatrix} | & | & | \\ \mathbf{G}_1 & \mathbf{G}_2 & \mathbf{G}_3 \\ | & | & | \end{pmatrix}.$$

Writing

$$\mathbf{w} = \begin{pmatrix} w_1 \\ w_2 \\ w_3 \\ w_4 \end{pmatrix} = \begin{pmatrix} \boldsymbol{\omega}_1 \\ \boldsymbol{\omega}_2 \end{pmatrix}$$

gives

$$G^\dagger \mathbf{w} = \begin{pmatrix} \boldsymbol{\gamma}_{1;1}^\dagger \boldsymbol{\omega}_1 + \boldsymbol{\gamma}_{1;2}^\dagger \boldsymbol{\omega}_2 \\ \boldsymbol{\gamma}_{2;1}^\dagger \boldsymbol{\omega}_1 + \boldsymbol{\gamma}_{2;2}^\dagger \boldsymbol{\omega}_2 \\ \boldsymbol{\gamma}_{3;1}^\dagger \boldsymbol{\omega}_1 + \boldsymbol{\gamma}_{3;2}^\dagger \boldsymbol{\omega}_2 \end{pmatrix} = \begin{pmatrix} \pi_1 \\ \pi_2 \\ \pi_3 \end{pmatrix}. \tag{B3}$$

With these preliminaries taken care of, we go on to calculate $\mathcal{I}$.

2. Calculating $\mathcal{I}$

We show how to calculate the matrix element $\mathcal{I}_{11}$. Calculation of the remaining three matrix elements is similar and so we simply quote the final result for these matrix elements at the end of this subsection.

From Eqs. (B1)–(B3) we have

$$\begin{aligned} \mathcal{I}_{11} &= (\mathbf{c}_1^\dagger \mathbf{e}_1)\pi_1 + (\mathbf{c}_1^\dagger \mathbf{f}_1)\pi_2 + (\mathbf{c}_1^\dagger \mathbf{g}_1)\pi_3 \\ &= w_1 \left[(\mathbf{c}_1^\dagger \mathbf{e}_1)(\mathbf{e}_1^\dagger \mathbf{c}_1) + (\mathbf{c}_1^\dagger \mathbf{f}_1)(\mathbf{f}_1^\dagger \mathbf{c}_1) + (\mathbf{c}_1^\dagger \mathbf{g}_1)(\mathbf{g}_1^\dagger \mathbf{c}_1) \right] \\ &\quad + w_2 \left[(\mathbf{c}_1^\dagger \mathbf{e}_1)(\mathbf{e}_1^\dagger \mathbf{c}_2) + (\mathbf{c}_1^\dagger \mathbf{f}_1)(\mathbf{f}_1^\dagger \mathbf{c}_2) + (\mathbf{c}_1^\dagger \mathbf{g}_1)(\mathbf{g}_1^\dagger \mathbf{c}_2) \right] \\ &\quad + w_3 \left[(\mathbf{c}_1^\dagger \mathbf{e}_1)(\mathbf{e}_2^\dagger \mathbf{c}_1) + (\mathbf{c}_1^\dagger \mathbf{f}_1)(\mathbf{f}_2^\dagger \mathbf{c}_1) + (\mathbf{c}_1^\dagger \mathbf{g}_1)(\mathbf{g}_2^\dagger \mathbf{c}_1) \right] \\ &\quad + w_4 \left[(\mathbf{c}_1^\dagger \mathbf{e}_1)(\mathbf{e}_2^\dagger \mathbf{c}_2) + (\mathbf{c}_1^\dagger \mathbf{f}_1)(\mathbf{f}_2^\dagger \mathbf{c}_2) + (\mathbf{c}_1^\dagger \mathbf{g}_1)(\mathbf{g}_2^\dagger \mathbf{c}_2) \right] \\ &= Tr \left[\begin{array}{c} \left(\mathbf{e}_1 \mathbf{e}_1^\dagger + \mathbf{f}_1 \mathbf{f}_1^\dagger + \mathbf{g}_1 \mathbf{g}_1^\dagger \right) \left(w_1 \mathbf{c}_1 \mathbf{c}_1^\dagger + w_2 \mathbf{c}_2 \mathbf{c}_1^\dagger \right) \\ + \left(\mathbf{e}_1 \mathbf{e}_2^\dagger + \mathbf{f}_1 \mathbf{f}_2^\dagger + \mathbf{g}_1 \mathbf{g}_2^\dagger \right) \left(w_3 \mathbf{c}_1 \mathbf{c}_1^\dagger + w_4 \mathbf{c}_2 \mathbf{c}_1^\dagger \right) \end{array} \right]. \end{aligned}$$

Inserting the various definitions from Appendix B 1 finally gives (after a moderate amount of algebra)

$$\mathcal{I}_{11} = w_1 - w_4. \tag{B4}$$

Similar calculations give:

$$\mathcal{I}_{21} = 2w_2 \tag{B5}$$

$$\mathcal{I}_{12} = 2w_3 \tag{B6}$$

$$\mathcal{I}_{22} = w_4 - w_1. \tag{B7}$$

This completes the derivation of Eq. (27).

Appendix C: Modeling phase noise effects

In this Appendix we present the noise model used to study the impact of phase jitter on the NOC improved TRP gates presented in Section III B 1. Appendix C 1 introduces the noise model and establishes key relations between the noise parameters; while Appendix C 2 describes how a realization of phase noise with arbitrary power is generated, as well as the protocol used to simulate the noisy Schrodinger gate dynamics.

1. Noise model

We start with a few basic facts about stationary random processes. The rate at which a noise field $N(t)$ can do work (i. e. noise power) is [37],

$$P = N^2(t),$$

and the energy that can be delivered in a time interval dt is,

$$dE = N^2(t)\, dt.$$

We consider power-type noise for which the time-averaged noise power

$$\overline{P} = \lim_{T\to\infty} \frac{1}{T} \int_{-T/2}^{T/2} N^2(t)\, dt \tag{C1}$$

is finite. The total noise energy

$$E = \int_{-\infty}^{\infty} dt\, N^2(t) \tag{C2}$$

diverges for this class of noise. The divergence is due to the occurrence of an infinite number of noise fluctuations in the time interval $-\infty < t < \infty$. The energy of an individual fluctuation is, however, finite.

The time-averaged noise power $\overline{P}$ can be related to the noise correlation function,

$$\overline{N(t)N(t-s)} \equiv \lim_{T\to\infty} \frac{1}{T} \int_{-T/2}^{T/2} dy\, N(y)N(y-s). \tag{C3}$$

Comparing Eqs. (C1) and (C3) we see that,

$$\overline{P} = \overline{N^2(t)}. \tag{C4}$$

The Weiner-Khintchine theorem [38] shows that the noise correlation function and the power spectral density $S_N(f)$ form a Fourier transform pair:

$$\overline{N(t)N(t-s)} = \int_{-\infty}^{\infty} df\, S_N(f)\, e^{-2\pi i f s}. \tag{C5}$$

Thus, it follows from Eqs. (C4) and (C5) that

$$\overline{P} = \int_{-\infty}^{\infty} df\, S_N(f), \tag{C6}$$

which identifies $S_N(f)$ as the mean noise power available in the frequency interval $(f,\, f + df)$.

In the remainder of this Appendix we focus on phase noise $\delta\phi(\tau)$, where τ is the dimensionless time introduced in Appendix A 1. We model this noise as shot noise which is a common type of electronic noise. The presentation extends earlier work in Ref. [39]. It is straight-forward to adapt the following development to treat other forms of noise.

As shot noise, the phase noise $\delta\phi(\tau)$ is produced by a sequence of randomly occurring noise fluctuations $F(t)$. The fluctuations: (1) occur independently of each other at average rate $\overline{n}$ per unit time; (2) are uniformly distributed over the time interval $[-\tau_0/2, \tau_0/2]$ of the TRP inversion; and (3) have a peak value x which is Gaussian distributed with mean $\overline{x} = 0$, variance $\overline{x^2} = \sigma^2$, and temporal width $2\tau_f$ which is the fluctuation lifetime. We assume that $2\tau_f$ is much shorter than the TRP inversion time τ_0. The bandwidth of $F(\tau)$ is thus $\Delta\omega \sim 1/2\tau_f$. Thus a realization of the phase noise has the form

$$\delta\phi(\tau) = \sum_{i=1}^{\mathcal{N}_f} F(\tau - \tau_i), \tag{C7}$$

where $\mathcal{N}_f$ denotes the number of noise fluctuations present (a stochastic variable), i labels the noise fluctuations, and τ_i specifies the center of the ith fluctuation. The mean number of fluctuations $\overline{\mathcal{N}_f}$ occurring in the time interval $[-\tau_0/2, \tau_0/2]$ is $\overline{\mathcal{N}_f} = \overline{n}\,\tau_0$. It is well-known that for noise with these properties, the actual number of fluctuations n that occur in a time τ_0 is governed by the Poisson distribution [40]:

$$p(n) = \frac{(\overline{\mathcal{N}_f})^n}{n!}\, e^{-\overline{\mathcal{N}_f}}.$$

The energy present in a single fluctuation is:

$$\varepsilon = \int_{-\infty}^{\infty} F^2(\tau)\, d\tau. \tag{C8}$$

Let $F(\tau) = xh(\tau)$, where $h(\tau)$ is any convenient function of finite support with normalization

$$\int_{-\infty}^{\infty} d\tau\, h^2(\tau) = 2\tau_f. \tag{C9}$$

As mentioned above, x is Gaussian distributed with mean $\overline{x} = 0$ and variance $\overline{x^2} = \sigma^2$. From Eq. (C8), $\varepsilon = 2x^2\,\tau_f$, and the mean energy per fluctuation $\overline{\varepsilon}$ is,

$$\overline{\varepsilon} = 2\,\overline{x^2}\,\tau = 2\sigma^2\,\tau. \tag{C10}$$

For shot noise, the power spectral density for $\delta\phi(\tau)$ is [41]

$$S_\phi(f) = \overline{n}\,|g(f)|^2, \tag{C11}$$

where $g(f)$ is the Fourier transform of the fluctuation profile $F(t)$. Thus, using Eqs. (C6), (C11), and Paresval's theorem gives,

$$\overline{P} = \overline{n} \int_{-\infty}^{\infty} d\tau\, F^2(\tau). \tag{C12}$$

Finally, using Eqs. (C8) and (C10) gives,

$$\overline{P} = 2\,\overline{n}\,\sigma^2\,\tau_f. \tag{C13}$$

Thus we see that our noise model is characterized by any three of the parameters $\overline{P}$, $\overline{n}$, σ^2, and τ_f.

We close this subsection by deriving an important connection between the mean noise power $\overline{P}$ and the phase jitter σ_ϕ introduced in Section III C 2. From Eq. (C7), we have

$$\delta\phi^2(\tau) = \sum_{i,j=1}^{\mathcal{N}_f} F(\tau - \tau_i)F(\tau - \tau_j). \tag{C14}$$

Averaging over the noise gives

$$\overline{\delta\phi^2(\tau)} = \overline{\mathcal{N}_f}\,\overline{F^2(\tau)}, \tag{C15}$$

where we have used the statistical independence of distinct noise fluctuations, and that $2\tau_f \ll \tau_0$. As in the proof of Campbell's theorem [42], it is possible to show that

$$\overline{F^2(\tau)} = \int_{-\infty}^{\infty} \frac{d\tau}{\tau_0}\, \sigma^2\, h^2(\tau), \tag{C16}$$

where, recall $F(\tau) = xh(\tau)$, and $\overline{x^2} = \sigma^2$. Inserting Eq. (C16) and $\sigma_\phi = \sqrt{\overline{\delta\phi^2(\tau)}}$ into Eq. (C15) gives

$$\sigma_\phi^2 = \frac{\overline{\mathcal{N}_f}}{\tau_0}\sigma^2 \int_{-\infty}^{\infty} d\tau\, h^2(\tau). \tag{C17}$$

Finally, inserting Eqs. (C9) and (C13), and $\overline{\mathcal{N}_f} = \overline{n}\tau_0$ into Eq. (C17) gives

$$\sigma_\phi = \sqrt{\overline{P}}. \tag{C18}$$

Thus the phase jitter σ_ϕ is simply another way to represent the phase noise power $\overline{P}$. Using Eq. (48), we can also express the timing jitter σ_t in terms of $\overline{P}$:

$$\sigma_t = \frac{\sqrt{\overline{P}}}{(2\pi f_{clock})}. \tag{C19}$$

2. Noisy simulation protocol

The numerical simulations used to study the impact of phase jitter on the NOC improved TRP gates constructs a realization of phase noise as follows. We first sample a positive integer $\mathcal{N}_f$ according to the Poisson distribution with mean $\overline{\mathcal{N}_f} = \overline{n}\,\tau_0$, where τ_0 is the (dimensionless) TRP inversion time. N_f corresponds to the number of

fluctuations present in the noise realization. The noise model assumes these fluctuations occur independently with probability $dp_f = (1/\tau_0)d\tau$. We sample $\mathcal{N}_f$ numbers τ_i $(i = 1, \cdots, \mathcal{N}_f)$ from the interval $(-\tau_0/2, \tau_0/2)$. The τ_i give the temporal centers of the $\mathcal{N}_f$ fluctuations. For simplicity, we assume that the fluctuation profile $h(\tau)$ is a square pulse of duration $2\tau_f$. We next carry out $\mathcal{N}_f$ samples x_i $(i = 1, \cdots, \mathcal{N}_f)$ of a Gaussian distribution with mean $\overline{x}_i = 0$ and variance $\overline{x_i^2} = \sigma^2$. Here x_i is the peak value of the ith fluctuation. These sample results produce the noise realization $\delta\Phi(\tau)$:

$$\delta\Phi(\tau) = \sum_{i=1}^{\mathcal{N}_f} x_i \left[\frac{\mathrm{sgn}(\tau - \tau_{il}) - \mathrm{sgn}(\tau - \tau_{ir})}{2} \right], \quad \text{(C20)}$$

where $\tau_{il} = \tau_i - \tau_f$, and $\tau_{ir} = \tau_i + \tau_f$. We shall need to produce noise realizations with arbitrary mean noise power $\overline{P}$. We do this by the following normalization procedure. First we calculate the mean noise power $\overline{\mathcal{P}}$ of the noise realization $\delta\Phi(\tau)$ just produced:

$$\overline{\mathcal{P}} = \frac{1}{\tau_0} \int_{-\tau_0/2}^{\tau_0/2} d\tau\, \delta\Phi^2(\tau). \quad \text{(C21)}$$

Then, if the desired value for the noise power is $\overline{P}$, we rescale $\delta\Phi(\tau)$ in Eq. (C20) so that $\delta\Phi(\tau) \to \delta\phi(\tau) \equiv \sqrt{\overline{P}/\overline{\mathcal{P}}}\,\delta\Phi(\tau)$. The result is a noise realization $\delta\phi(\tau)$ with mean noise power $\overline{P}$. The simulation takes as inputs the mean noise power $\overline{P}$, the standard deviation $\sqrt{\overline{x_i^2}} = \sigma$, and τ_f which is half the fluctuation lifetime. The fluctuation rate $\overline{n}$ then follows from Eq. (C13): $\overline{n} = \overline{P}/(2\sigma^2\tau_f)$. In all the one (two) qubit gate simulations, we used $\sigma = 0.1$ (0.1) and $\tau_f = 0.3$ (0.1). All one-qubit gates were run at mean noise power $\overline{P} = 0.001, 0.008$ corresponding to timing jitter $\sigma_t = 5.03\text{ps}, 14.2\text{ps}$, respectively. The Hadamard gate was run at seven other values of $\overline{P}$ to produce the data displayed in Figure 3. The two-qubit gate was run at $\overline{P} = 0.001, 0.005$ corresponding to timing jitter $\sigma_t = 5.03\text{ps},\ 11.3\text{ps}$.

For a given target gate, and given values of $(\overline{P}, \sigma, \tau_f)$, ten phase noise realizations $\delta\phi(\tau)$ were generated. For each realization, the phase noise was added to the TRP twist phase $\phi_4(\tau)$, and the resulting noisy twist phase $\phi_4'(\tau)$ caused the noisy TRP control field $\mathbf{F}_0'(\tau)$ to twist incorrectly, as described in Section III C 2. For each noise realization: (i) the state trajectory $U(\tau)$ was determined by numerically simulating the Schrodinger dynamics generated by the noisy control field $\mathbf{F}'(\tau) = \mathbf{F}_0'(\tau) + \Delta\mathbf{F}(\tau)$ (see Section III C 2); and (ii) used to determine the $Tr\,P$ upper bound for the gate error probability P_e. Using the ten values of $Tr\,P$ obtained from the simulations, the average $\langle Tr\,P\rangle$ and standard deviation $\sigma(TrP)$ were then calculated and the noise-averaged NOC gate performance was then approximated by $P_e \le \langle Tr\,P\rangle \pm \sigma(TrP)$. The results of these simulations appear in Section III C 2 and Appendix D.

Appendix D: Results for remaining quantum gates

In Sections III B and III C we presented our numerical simulation results for the TRP-NOC improved approximation to the Hadamard gate. In this Appendix we present our results for the remaining quantum gates in the universal gate set $\mathcal{G}_U$ introduced in Section III A 2. These are the one-qubit NOT, modified phase, and modified $\pi/8$ gates, and the two-qubit modified controlled-phase gate. We present the NOC performance gains for ideal control in Appendix D 1, and in Appendix D 2 examine the robustness of these gains to: (i) control parameters with finite precision; and (ii) timing/phase jitter. As our discussion closely follows that in Sections III B and III C, a more abbreviated discussion will be given here.

1. Ideal control

For each one-qubit gate in $\mathcal{G}_U$, the nominal Hamiltonian $H_0^1(\tau)$ (see Eq. (45)) is determined by the corresponding values of λ and η_4 appearing in Table VII and the dimensionless TRP inversion time $\tau_0 = 160$. With $H_0^1(\tau)$, the numerical simulation procedure described in Section III A 3 for Strategy 1 was implemented to determine the $Tr\,P$ upper bound on the gate error probability $P_e \le Tr\,P$. For the two-qubit modified controlled-phase gate, the two-qubit nominal Hamiltonian $H_0^2(\tau)$ (see Eq. (46)) is determined by the control parameters appearing in Table VIII and the dimensionless TRP inversion time $\tau_0 = 120$. For Strategy 2 , Step 2 of the six step numerical procedure requires the three matrices $\mathcal{G}_1$, $\mathcal{G}_2$, and $\mathcal{G}_3$. These follow from the functional derivatives of $H_0^2(\tau)$ with respect to the components of the control field $\mathbf{F}(\tau)$:

$$\begin{cases} \mathcal{G}_1 = d_3 \left[\cos\left((\frac{d_1 b_2}{b_1 - b_2} + d_1)\tau \right) \sigma_x^1 + \sin\left((\frac{d_1 b_2}{b_1 - b_2} + d_1)\tau \right) \sigma_y^1 \right] \\ \qquad + \left[\cos\left((\frac{d_1 b_2}{b_1 - b_2})\tau \right) \sigma_x^2 + \sin\left((\frac{d_1 b_2}{b_1 - b_2})\tau \right) \sigma_y^2 \right] \\ \mathcal{G}_2 = d_3 \left[\cos\left((\frac{d_1 b_2}{b_1 - b_2} + d_1)\tau \right) \sigma_y^1 - \sin\left((\frac{d_1 b_2}{b_1 - b_2} + d_1)\tau \right) \sigma_x^1 \right] \\ \qquad + \left[\cos\left((\frac{d_1 b_2}{b_1 - b_2})\tau \right) \sigma_y^2 - \sin\left((\frac{d_1 b_2}{b_1 - b_2})\tau \right) \sigma_x^2 \right] \\ \mathcal{G}_3 = d_3 \sigma_z^1 + \sigma_z^2 \end{cases} \quad \text{(D1)}$$

As noted in Step 3 of the procedure for Strategy 2, we chose $R(\tau) = I_{3\times 3}$ and $S(\tau) = I_{16\times 16}$, where $I_{n\times n}$ is the $n \times n$ identity matrix. Satisfying the Ricatti equation then required $Q(\tau) = G(\tau)G^\dagger(\tau)$. Carrying out the remaining steps in the numerical procedure for Strategy 2

leads to the $Tr\,P$ upper bound for the gate error probability P_e. The simulation results for all gates in the universal set $\mathcal{G}_U$ appear in Table I (see Section III B 1). We see that for all one-qubit gates in $\mathcal{G}_U$, NOC reduced the gate error probability P_e by *four orders-of-magnitude* (viz. $10^{-4} \rightarrow 10^{-8}$), while for the two-qubit gate, P_e was reduced by *two orders-of-magnitude* (viz. $10^{-3} \rightarrow 10^{-5}$). NOC has thus substantially improved TRP gate performance, producing gates with error probabilities falling well below the target accuracy threshold of 10^{-4}. Because P_e is so small for the one-qubit gates, we do not write out the unitary matrix produced by NOC as they each agree with their corresponding target gate U_{tgt} to six significant figures. For the two-qubit modified controlled-phase gate, the unitary gate produced is:

$$Re(V_{cp}) = \begin{pmatrix} 1.0000 & 0.0001 & 0.0000 & 0.0024 \\ 0.0000 & 1.0000 & -0.0001 & 0.0000 \\ 0.0001 & 0.0001 & -1.0000 & -0.0001 \\ -0.0024 & 0.0000 & 0.0000 & 1.0000 \end{pmatrix};$$

$$Im(V_{cp}) = \begin{pmatrix} 0.0055 & 0.0001 & 0.0000 & -0.0016 \\ -0.0001 & 0.0014 & 0.0004 & 0.0000 \\ -0.0001 & -0.0004 & 0.0003 & 0.0000 \\ -0.0017 & 0.0000 & 0.0000 & 0.0015 \end{pmatrix}.$$

The reader can directly examine the NOC improvement in V_{cp} by comparing the above unitary gate with that found in Ref. [15] which was reproduced in Appendix A 3.

We now determine the amount of bandwidth needed to realize these NOC performance improvements. The following calculations assume the TRP inversion time for a one-qubit gate is 1μs and for the two-qubit gate is 5μs. Recall that the (dimensionless) bandwidth was estimated by determining the frequency $\omega_{0.1}$ at which $\Delta\mathcal{F}_x(\omega)$ is 10% of the peak value$\Delta\mathcal{F}_x(0)$. For the one-qubit gates, Eq. (47) then determined the dimensionful bandwidth $\overline{\omega}_{0.1}$. For the two-qubit gate, whose dimensionless TRP inversion time is $\tau_0 = 120$, the connection between dimensionful and dimensionless bandwidth is

$$\frac{\overline{\omega}_{0.1}}{\omega_{0.1}} = \frac{120}{5\mu\text{s}} = 24 \text{ MHz}. \qquad \text{(D2)}$$

With these preliminaries out of the way, we present our bandwidth results for the gates in $\mathcal{G}_U$.

1. Hadamard gate: This gate was considered in Section III B 2. The (dimensionful) bandwidth found there is $\overline{\omega}_{0.1} = 640$ MHz.

2. NOT gate: Figure 4 shows the x-component of the control field modification $\Delta F_x(\tau)$ as a function of the dimensionless time τ for the NOT gate. Figure 5 shows its Fourier transform $\Delta\mathcal{F}_x(\omega)$. Examination of the data used to produce Figure 5 gives $\omega_{0.1} = 0.8$. Eq. (47) then gives a dimensionful bandwidth of $\overline{\omega}_{0.1} = 130$ MHz.

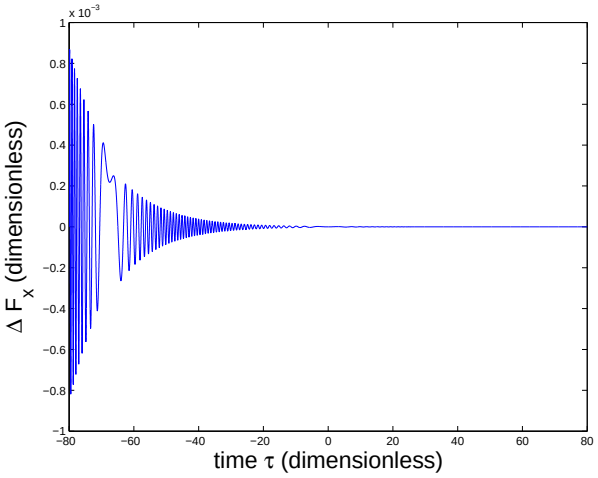

FIG. 4: (Color online) The x-component of the control field modification $\Delta F_x(\tau)$ for the NOT gate.

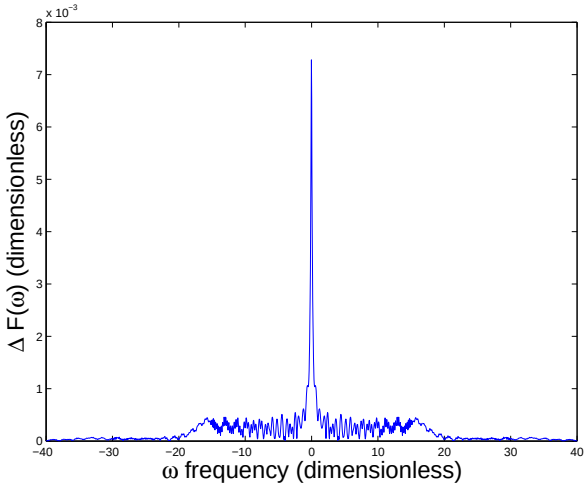

FIG. 5: (Color online) The Fourier transform of the x-component of the control field modification $\Delta\mathcal{F}_x(\omega)$ for the NOT gate.

3. Modified phase gate: Figure 6 shows the x-component of the control field modification $\Delta F_x(\tau)$ as a function of the dimensionless time τ for the modified phase gate. Figure 7 shows its Fourier transform $\Delta\mathcal{F}_x(\omega)$. Examination of the data used to produce Figure 7 gives $\omega_{0.1} = 1.9$, which, using Eq. (47), gives a dimensionful bandwidth of $\overline{\omega}_{0.1} = 300$ MHz.

4. Modified $\pi/8$ gate: Figure 8 shows the x-component of the control field modification $\Delta F_x(\tau)$ as a function of the dimensionless time τ for the modified $\pi/8$ gate. Figure 9 shows its Fourier transform $\Delta\mathcal{F}_x(\omega)$. Examination of the data used to produce Figure 9 gives $\omega_{0.1} = 1.3$, which, using Eq. (47), gives a dimensionful bandwidth of $\overline{\omega}_{0.1} = 210$ MHz.

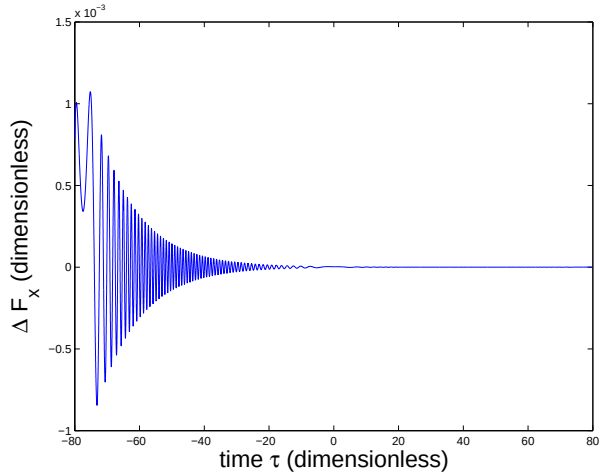

FIG. 6: (Color online) The x-component of the control field modification $\Delta F_x(\tau)$ for the modified phase gate

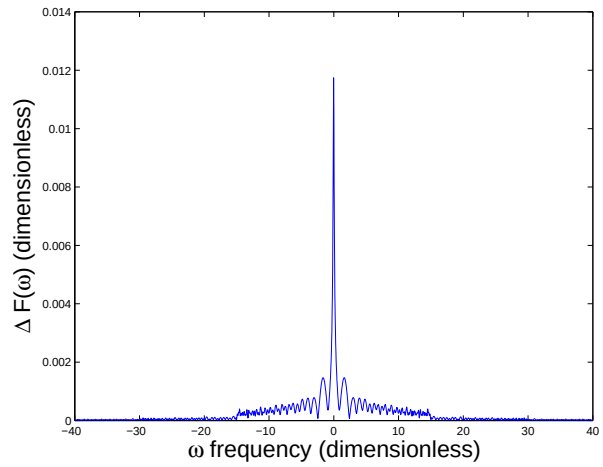

FIG. 7: (Color online) The Fourier transform of the x-component of the control field modification $\Delta\mathcal{F}_x(\omega)$ for the modified phase gate.

5. Modified controlled-phase gate: Figure 10 shows the x-component of the control field modification $\Delta F_x(\tau)$ as a function of the dimensionless time τ for the modified controlled-phase gate. Figure 11 shows its Fourier transform $\Delta\mathcal{F}_x(\omega)$. Examination of the data used to produce Figure 11 gives $\omega_{0.1} = 34$, which, using Eq. (D2), gives a dimensionful bandwidth of $\overline{\omega}_{0.1} = 820$ MHz.

Table II (see Section III B 2) collects the bandwidth results for all gates in $\mathcal{G}_U$. As noted there, AWGs with 5GHz bandwidth are commercially available so that the bandwidth requirements for NOC are within the range of existing commercially available AWGs.

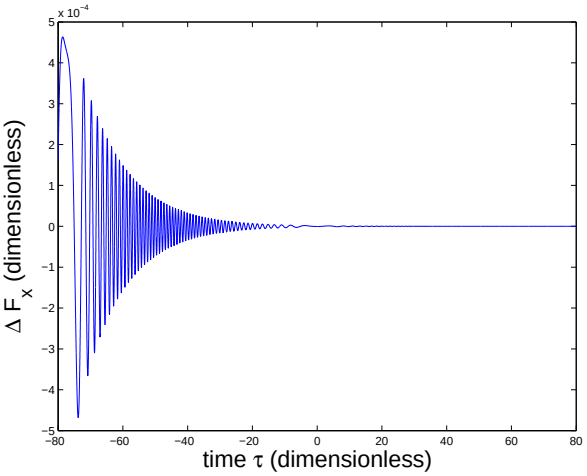

FIG. 8: (Color online) The x-component of the control field modification $\Delta F_x(\tau)$ for the modified $\pi/8$ gate.

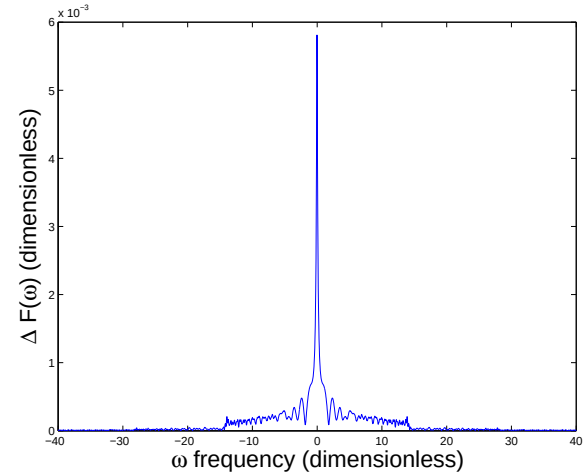

FIG. 9: (Color online) The Fourier transform of the x-component of the control field modification $\Delta\mathcal{F}_x(\omega)$ for the modified $\pi/8$ gate.

2. Robustness to imperfect control

In this subsection we examine the robustness of the non-Hadamard gates in $\mathcal{G}_U$ to: (i) control parameters with finite-precision (Appendix D 2 a); and (ii) phase/timing jitter (Appendix D 2 b). The same issues were examined for the Hadamard gate in Section III C 2.

a. Finite-precision control parameters

As with the discussion of the Hadamard gate in Section III C 1, here we determine the minimum control parameter precision needed to realize the NOC perfor-

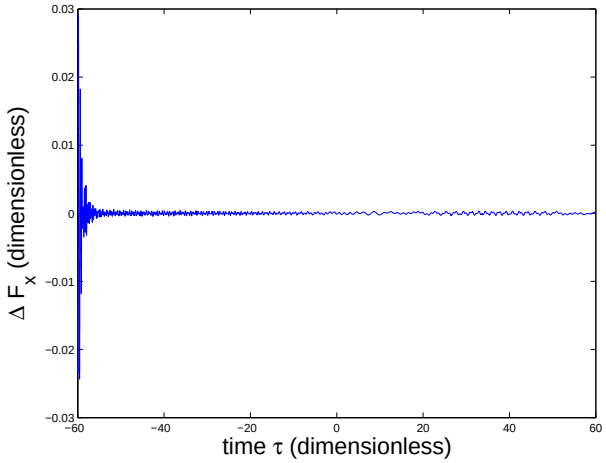

FIG. 10: (Color online) The x-component of the control field modification $\Delta F_x(\tau)$ for modified controlled-phase gate,

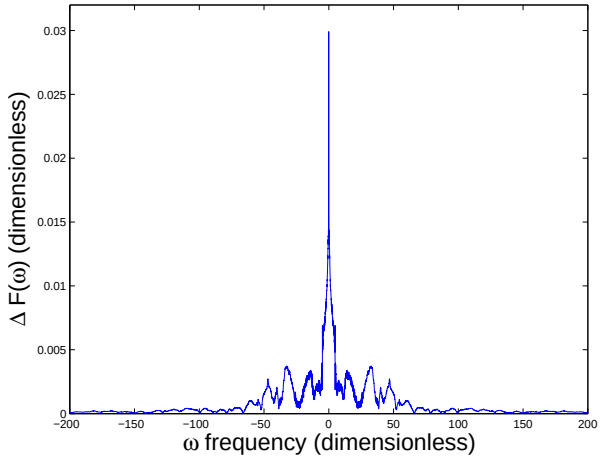

FIG. 11: (Color online) The Fourier transform of the x-component of the control field modification $\Delta\mathcal{F}_x(\omega)$ for the modified controlled-phase gate.

mance improvements found for the non-Hadamard gates in $\mathcal{G}_U$ in Appendix D 1. For the one-qubit gates, the NOC performance improvements were found to be most sensitive to small changes in η_4. Thus we will only show how the $Tr\,P$ upper bound on the gate error probability P_e varied as we changed η_4 by one in its least significant digit. For the two-qubit modified controlled-phase gate, performance was most sensitive to small changes in d_1, d_4, and c_4. We only show results for d_1 as similar results are found for d_4 and c_4.

1. NOT gate: For the NOT gate, NOC delivered a gate with $P_e \leq 8.58 \times 10^{-9}$. In Table IX we show how the $Tr\,P$ upper bound on the gate error probability ($P_e \leq Tr\,P$) changes due to a small shift in η_4 away from its optimum value. We show the variation in $Tr\,P$ when the NOC modification is both included and omitted. As with the Hadamard gate, η_4 must be controlled to better than one part in $10,000$ to realize the NOC performance gains. As shown in the Hadamard gate discussion, this is possible using an AWG with at least 14-bit vertical resolution. Using less precision will give rise to uncertainty in the fourth significant digit, and to a washing out of the NOC performance gains.

TABLE IX: Sensitivity of TrP to a small variation of η_4 away from its optimum value for the one-qubit NOT gate. For all η_4 values, λ is maintained at its optimum value $\lambda = 6.965$. Column 2 (3) shows the variation of $Tr\,P$ when the control field includes (omits) the NOC modification $\Delta\mathbf{F}(\tau)$. Recall that $Tr\,P$ upper bounds the gate error probability $P_e \leq Tr\,P$.

η_4	TrP (with NOC)	TrP (without NOC)
2.188×10^{-4}	6.50×10^{-3}	1.55×10^{-2}
2.189×10^{-4}	8.58×10^{-9}	6.27×10^{-5}
2.190×10^{-4}	9.80×10^{-3}	3.28×10^{-2}

2. Modified $\pi/8$ gate: For the modified $\pi/8$ gate, NOC delivered a gate with $P_e \leq 1.06 \times 10^{-8}$. In Table X we show how the $Tr\,P$ upper bound on the gate error probability ($P_e \leq Tr\,P$) changes due to a small shift in η_4 away from its optimum value. We show the variation in $Tr\,P$ when the NOC modification is both included and omitted. As with the Hadamard gate, η_4 must be controlled to better than one part in $10,000$ to realize the NOC performance gains. This is possible using an AWG with at least 14-bit vertical resolution. Using less precision will give rise to uncertainty in the fourth significant digit, and to a washing out of the NOC performance gains.

TABLE X: Sensitivity of TrP to a small variation of η_4 away from its optimum value for the one-qubit modified $\pi/8$ gate. For all η_4 values, λ is maintained at its optimum value $\lambda = 8.465$. Column 2 (3) shows the variation of $Tr\,P$ when the control field includes (omits) the NOC modification $\Delta\mathbf{F}(\tau)$. Recall that $Tr\,P$ upper bounds the gate error probability $P_e \leq Tr\,P$.

η_4	TrP (with NOC)	TrP (without NOC)
1.674×10^{-4}	7.10×10^{-3}	4.99×10^{-2}
1.675×10^{-4}	1.06×10^{-8}	2.13×10^{-4}
1.676×10^{-4}	7.30×10^{-3}	3.90×10^{-2}

3. Modified phase gate: For the modified phase gate, NOC delivered a gate with $P_e \leq 1.08 \times 10^{-8}$. In Table XI we show how the $Tr\,P$ upper bound on the gate error probability ($P_e \leq Tr\,P$) changes due to a small shift in η_4 away from its optimum value. We show

TABLE XI: Sensitivity of TrP to a small variation of η_4 away from its optimum value for the one-qubit modified phase gate. For all η_4 values, λ is maintained at its optimum value $\lambda = 8.073$. Column 2 (3) shows the variation of $Tr\,P$ when the control field includes (omits) the NOC modification $\Delta\mathbf{F}(\tau)$. Recall that $Tr\,P$ upper bounds the gate error probability $P_e \leq Tr\,P$.

η_4	TrP (with NOC)	TrP (without NOC)
1.665×10^{-4}	1.20×10^{-3}	4.42×10^{-2}
1.666×10^{-4}	1.08×10^{-8}	4.62×10^{-4}
1.667×10^{-4}	6.10×10^{-3}	5.74×10^{-2}

the variation in $Tr\,P$ when the NOC modification is both included and omitted. As with the Hadamard gate, η_4 must be controlled to better than one part in $10,000$ to realize the NOC performance gains. This is possible using an AWG with at least 14-bit vertical resolution. Using less precision will give rise to uncertainty in the fourth significant digit, and to a washing out of the NOC performance gains.

4. Modified controlled-phase gate: For the two-qubit modified controlled-phase gate, NOC delivered a gate with $P_e \leq 5.21 \times 10^{-5}$. In Table XII we show how the $Tr\,P$ upper bound on the gate error probability ($P_e \leq Tr\,P$) changes due to a small shift in d_1 away from its optimum value. We show the variation in $Tr\,P$ when the NOC modification is both included and omitted. We see that d_1 must be controlled to better than one part in $100,000$ to realize the NOC performance gains. Such control parameter precision is attainable using an AWG with 17-bit vertical resolution (viz. one part in $2^{17} = 131,072$). We are not aware of such AWGs being commercially available, thus requiring custom electronics to realize the NOC performance gains for this two-qubit gate. Note that 16-bit precision corresponds to a precision of one part in $2^{16} = 65,536$, and so to an uncertainty in the fifth significant digit. Thus with less than 17-bits of precision, Table XII indicates that the NOC performance gains will be washed out by the uncertainty in the least significant digit of d_1. Similar results are found for d_4 and c_4.

TABLE XII: Sensitivity of TrP to a small variation of d_1 away from its optimum value for the two-qubit modified controlled-phase gate. For all d_1 values, the remaining control parameters appearing in Table VIII are maintained at the optimum values given there. Column 2 (3) shows the variation of $Tr\,P$ when the control field includes (omits) the NOC modification $\Delta\mathbf{F}(\tau)$. Recall that $Tr\,P$ upper bounds the gate error probability $P_e \leq Tr\,P$.

d_1	TrP (with NOC)	TrP (without NOC)
11.701	1.16×10^{-3}	3.36×10^{-3}
11.702	5.21×10^{-5}	1.27×10^{-3}
11.703	1.16×10^{-3}	1.43×10^{-3}

b. Phase/timing jitter

In Section III C 2 we discussed the effects of timing/phase jitter on the NOC performance gains shown in Table I of Section III B 1. Appendix C introduced our model for phase noise and detailed the protocol for the numerical simulation of the NOC gate dynamics in the presence of such noise. Table V presented the simulation results for all gates in $\mathcal{G}_U$ for timing jitter $\sigma_t = 5$ps, the same as found in commercially available AWGs [34]. The Hadamard gate was discussed in Section III C 2 and similar remarks apply to the other gates in $\mathcal{G}_U$. The noise power corresponding to 5ps timing jitter at a clock frequency $f_{clock} = 1$GHz is $\overline{P} = 0.001$. As discussed in Appendix C 2, the one-qubit simulations used noise fluctuation parameters $\sigma = 0.1$ and $\tau_f = 0.3$, while the two-qubit simulations used $\sigma = 0.1$ and $\tau_f = 0.1$. From Appendix C 1, this corresponds to an average noise fluctuation rate $\overline{n} = \overline{P}/(2\sigma^2\tau_f) = 0.167$ (0.500) for the one-qubit (two-qubit) gate simulations. Thus for the one-qubit (two-qubit) gates with TRP (dimensionless) inversion time $\tau_0 = 160$ (120), each phase noise realization contained, on average, $\mathcal{N}_f = 27$ (60) noise fluctuations.

In Table XIII we present further noisy simulation results for all gates in $\mathcal{G}_U$ at noise power $\overline{P} = 0.005$ (0.008) for the two-qubit (one-qubit) gate(s). This corresponds, respectively, to: (i) timing jitter $\sigma_t = 11.3$ (14.2)ps; (ii) $\overline{n} = 2.50$ (1.33); and (iii) phase noise realizations with, on average, $\mathcal{N}_f = 300$ (213) noise fluctuations. We see that the increased noise power $\overline{P} = 0.001 \to 0.005, 0.008$ only degraded the NOC performance gains slightly more than was seen in Table V. Notice that, even with phase jitter that is worse than occurs in commercially available AWGs, all gates in $\mathcal{G}_U$ still have error probabilities that fall below the target accuracy threshold of 10^{-4}.

[1] D. Aharanov and M. Ben-Or, in Proceedings of the Twenty-Ninth ACM Symposium on the Theory of Computing, 176 (1997).

[2] A. Y. Kitaev, Russ. Math. Surv. **52**, 1191 (1997).

[3] A. Y. Kitaev, in Quantum Communication, Computing, and Measurement (Plenum Press, New York, 1997), pp. 181–188.

[4] D. Gottesman, Ph. D. thesis, California Institute of Tech-

TABLE XIII: Sensitivity of TrP to timing jitter $\sigma_t = \sqrt{\overline{P}}/(2\pi f_{clock})$ for all target gates in the universal set $\mathcal{G}_U$. For all one-qubit (two-qubit) gates, the numerical simulations used mean noise power $\bar{P} = 0.008$ (0.005), which corresponds to timing jitter $\sigma_t = 14.2$ (11.3)ps for $f_{clock} = 1$GHz. For each gate, ten phase noise realizations were generated (see Appendix C), leading to ten values of the $Tr\,P$ upper bound on the gate error probability $P_e \leq Tr\,P$. The third column lists, for each gate, the corresponding average $< TrP >$, and uses the standard deviation $\sigma(TrP)$ to indicate the spread of $Tr\,P$ about the average.

Gate	Timing-jitter σ_t	$P_e \leq\ < TrP > \pm\sigma$(TrP) with NOC
Hadamard	$14.2ps$	$(5.58 \pm 2.55) \times 10^{-5}$
NOT	$14.2ps$	$(5.71 \pm 2.67) \times 10^{-5}$
Modified phase	$14.2ps$	$(7.09 \pm 3.23) \times 10^{-5}$
Modified $\pi/8$	$14.2ps$	$(8.04 \pm 2.43) \times 10^{-5}$
Modified controlled phase	$11.3ps$	$(6.74 \pm 1.09) \times 10^{-5}$

nology, Pasadena, CA (1997).

[5] E. Knill, R. Laflamme, and W. H. Zurek, Science **279**, 342 (1998).

[6] E. Knill, R. Laflamme, and W. H. Zurek, Proc. R. Soc. Lond. A **454**, 365 (1998).

[7] J. Preskill, Proc. R. Soc. Lond. A **454**, 385 (1998).

[8] F. Gaitan, *Quantum error correction and fault-tolerant quantum computing* (CRC Press, Boca Raton, FL 2008).

[9] Robert F. Stengel, *Optimal control and estimation* (Dover Publications, Inc., New York 1994).

[10] F. Gaitan, Phys. Rev. A **68** 052314 (2003).

[11] J. W. Zwanziger, U. Werner-Zwanziger, and F. Gaitan, Chem. Phys. Lett. **375** 429 (2003).

[12] F. Gaitan, J. Mod. Opt. **51**, 2415 (2004).

[13] R. Li and F. Gaitan, Optics and Spectroscopy **99**, 257 (2005).

[14] R. Li, M. Hoover, and F. Gaitan, Quantum Info. Comp. **7** 594 (2007).

[15] R. Li, M. Hoover, and F. Gaitan, Quantum Info. Comp. **9** 290 (2009).

[16] R. Li and F. Gaitan, Quantum Info. Comp. **10**, 936 (2010).

[17] R. Li and F. Gaitan, J. Mod. Opt. **58**, 1922 (2011).

[18] E. Dennis, A. Kitaev, A. Landahl, and J. Preskill, J. Math. Phys. **43**, 4452 (2002).

[19] R. Raussendorf and J. Harrington, Phys. Rev. Lett. **98**, 190504 (2007).

[20] H. G. Katzgraber, H. Bombin, and M. A. Martin-Delgado, Phys. Rev. Lett. **103**, 090501 (2009).

[21] D. S. Wang, A. G. Fowler, C. D. Hill, and L.C.L. Hollenberg, Quant. Inf. Comp. **10**, 780 (2010).

[22] J. Ghosh, A. G. Fowler, and M. R. Geller, Phys. Rev. A **86**, 062318 (2012).

[23] We will spell out what we mean by "good approximation" in Section III.

[24] Value functions can also be considered with optimal assignments producing maximum value.

[25] For our purposes, it is sufficient that $Q(t)$ be a positive Hermitian matrix.

[26] As will be discussed in Section III A 3 and Appendix A 1, the numerical simulations transform the dimensionful Schrodinger equation into dimensionless form so that the time parameter in the simulations is dimensionless. When discussing Strategy 1 in Section II D the time t is actually dimensionless time. Thus when we say that the one-qubit numerical simulations have $T = 160$ we are making a statement about the dimensionless time parameter. The connection between dimensionful and dimensionless parameters is explained in Section III A 3 and Appendix A 1.

[27] A. Abragam, *Principles of nuclear magnetism* (Oxford University Press, New York 1961).

[28] F. Gaitan, J. Mag. Reson. **139** 152(1999).

[29] R. P. Feynman and A. R. Hibbs, *Quantum mechanics and path integrals*, (McGraw-Hill, New York, 1965).

[30] To achieve this level of gate performance required TRP sweep parameter values with 17-bits of precision. Ref. [16] modified the optimization cost function to reward both gate robustness and low error probability, and found TRP sweep parameter values that produced one-qubit TRP gates with $P_e < 4.62 \times 10^{-4}$, while only requiring sweep parameters with 14-bits of precision. This approach improved gate robustness at the cost of a small increase in the gate error probability. By showing how to interleave a TRP sweep with a suitable dynamical decoupling sequence, Ref. [17] was able to reduce the gate error probability for the two-qubit modified controlled phase gate to $P_e < 8.87 \times 10^{-5}$, while only requiring TRP sweep parameters with 14-bits of precision. This improved performance was achieved at the cost of a more complicated control field.

[31] The accuracy threshold theorem (ATT) requires $P_e < P_a$ for every application of a quantum gate. By defining P_e to be the worst-case value of $P_e(\psi)$ we insure that if $P_e < P_a$, then for every initial state ψ (and thus for every gate application), $P_e(\psi) < P_a$ as demanded by the ATT. However, if P_e is defined as an average-case value, states could exist for which $P_e(\psi) > P_a$ even though $P_e < P_a$. Such states would violate a core requirement of the ATT, and thus nullify its conclusion. It is not enough to satisfy the conditions of the ATT on average. Thus, in the context of fault-tolerant quantum computing, it is more appropriate to define the gate error probability as a worst-case value rather than as an average-case value.

[32] For example, the Agilent M8190A 12 GSa/s Arbitrary Waveform Generator provides 5 GHz bandwidth.

[33] For example, the Tektronix AWG5000B arbitrary waveform generator provides 14-bit vertical resolution.

[34] For example, the Tektronix AWG5000 arbitrary waveform generator has 5ps timing jitter.

[35] J. W. Zwanziger, S. P. Rucker, and G. C. Chingas, Phys. Rev. A **43**, 3232 (1991).
[36] Note that Refs. [14]–[17] have a factor of two error in the quoted value of τ_0 for the one-qubit gates. The correct value for these gates is $\tau_0 = 160$, as given here.
[37] J. B. Thomas, *Statistical Communication Theory* (Wiley, New York, 1969).
[38] F. Rief, *Fundamentals of Statistical and Thermal Physics* (McGraw-Hill, New York, 1965).
[39] F. Gaitan, Int. J. Quantum Inform. **4**, 483 (2006).
[40] A. W. Drake, *Fundamentals of Applied Probability Theory* (McGraw-Hill, New York, 1967).
[41] S. O. Rice, Bell Sys. Tech. J. **23**, 282 (1944).
[42] See Ref. [41], Section 1.3.